Next-Generation Mapping of the ACINUS-Mediated Alternative Splicing Machinery and Its Regulation by O-glycosylation in *Arabidopsis*

Ruben Shrestha[1]*, Andres V Reyes[1]*, Shane Carey[1]*, Sumudu S Karunadasa[1]*, Wenxuan Zhai [1], Danbi Byun[1], Wen-Dar Lin[2], Jie Li[3], Kathrine Alerte[1], Hongchang Cui[3], Zhi-Yong Wang[1], Shou-Ling Xu[1#]

[1] Department of Plant Biology, Carnegie Institution for Science, Stanford, CA, USA.

[2] Institute of Plant and Microbial Biology, Academia Sinica, 115 Taipei, Taiwan.

[3] Department of Biological Science, Florida State University, Tallahassee, Florida 32306, USA.

*These authors contributed equally.

#Corresponding author: Shouling Xu, slxu@stanford.edu

Abstract

Alternative splicing (AS) is a key mechanism of gene regulation, but the full repertoire of proteins involved and the regulatory mechanisms governing this process remain poorly understood. Using TurboID-based proximity labeling coupled with mass spectrometry (PL-MS), we comprehensively mapped the Arabidopsis AS machinery, focusing on the evolutionarily conserved splicing factor ACINUS, its paralog PININ, and the stable interactor SR45. We identified 298 high-confidence components, including both established and novel interactors, providing strong evidence that alternative splicing is coupled to transcription and that multiple RNA processing steps occur simultaneously in plants. Selected interactors were validated through AS readouts and phenotypic analysis. Furthermore, a systematic evaluation of O-glycosylation double mutants revealed that SECRET AGENT (O-GlcNAc transferase) and SPINDLY (O-fucose transferase) modulate AS through both ACINUS-dependent and -independent pathways. Our results unravel the plant AS network and highlight the global role of sugar modification in RNA processing.

Introduction

Alternative splicing (AS) is a key mechanism of gene regulation in both animals and plants[1]. During AS, the splicing machinery removes the introns by selecting from competing splice sites within the pre-mRNA, which is controlled by interactions between cis-acting elements and trans-acting factors, such as RNA-binding proteins (RBPs) and splicing factors. In a context-dependent manner, these factors either promote or inhibit splice site recognition and spliceosome assembly. AS generates multiple mRNA variants and protein isoforms from a single gene, affecting approximately 95% of genes in animals and 70% in plants[2-5].

The biological importance of AS has been demonstrated in several species. In flies, AS is essential for sex determination[6], while in humans it plays a critical role in tissue and organ development[7,8], with its dysregulation often associated with diseases such as cancer[9-11]. In plants, AS is critical for establishing tissue identity, enhancing immunity, and responding to environmental changes and developmental signals[5,12-15].

Characterization of the proteins that control AS is essential for understanding how this complex system accurately distinguishes between multiple, often similar, splice sites to precisely remove the introns. The spliceosome, the molecular machinery responsible for splicing, is one of the most sophisticated megadalton complexes in eukaryotic cells. It orchestrates two transesterification reactions that result in lariat formation, intron removal, and exon ligation. The spliceosome consists of five small nuclear RNAs (snRNAs) that assemble with proteins to form small nuclear ribonucleoproteins (snRNPs), along with hundreds of additional proteins, including non-snRNP splicing factors, cofactors and regulatory proteins[16]. Despite extensive research ranging from proteomic analyses using immunoprecipitations to systematic gene silencing/knockout using RNAi or CRISPR-Cas approaches, the complete composition and dynamic behavior of the spliceosome remain incompletely elucidated[17-19].

While the core components of the splicing machinery, such as snRNPs and certain non-snRNP proteins, are highly conserved among eukaryotes, AS exhibits both conserved[20] and species-specific features[21]. A key difference is intron length: Arabidopsis introns are significantly shorter (median length of 100 nucleotides)[22] than human introns (median length of 1.5-1.7 kb)[19,23]. This disparity likely reflects differences in the mechanisms of snRNP and SR proteins binding to pre-mRNA. In Arabidopsis, it has been suggested that the splicing machinery predominantly uses intron definition, where the splicesome first recognizes and assembles across introns. In contrast, exon definition, where the splicesome first recognizes and assembles across exons - is more common in humans[19]. These mechanistic differences correlate with different patterns of AS: in plants, intron retention is the most common form of AS, whereas in humans, exon skipping is the dominant AS event [5,24,25]. A comprehensive understanding of the proteins involved in plant AS will provide crucial insights into the mechanisms and evolution of AS.

Post-translational modifications (PTMs), such as phosphorylation, have been shown to play a critical role in the regulation of AS[26,27]. In addition to phosphorylation, our results indicate that several splicing factors are modified by O-GlcNAcylation and O-fucosylation[28-30]. qPCR data reveal AS defects in a few genes in single mutants of the O-GlcNAc transferase SECRET AGENT (SEC) and the O-fucose transferase SPINDLY (SPY) single mutants[13], suggesting that O-Glycosylation plays a role in AS regulation. However, a comprehensive evaluation of the global effects of SEC and SPY on AS, including analysis of double mutants, is still lacking. Such studies are needed to elucidate the role of O-GlcNAcylation and O-fucosylation in AS regulation.

Previously, we identified the evolutionarily conserved splicing factor ACINUS and its paralog PININ as key regulators of transcription, AS, and developmental transitions[13]. In this study, we used TurboID, an engineered high-activity biotin ligase[31,32], to comprehensively map ACINUS-mediated AS complexes. By constructing a high-confidence network centered on three baits - ACINUS, PININ and the stable interactor SR45- we characterized the composition of the AS machinery and identified both established and novel interactors. We validated the phenotypic readouts of several interactors, using either molecular readouts (alternative splicing defects) or morphological phenotypes. We further uncovered the roles of O-GlcNAcylation and O-fucosylation in regulating AS and transcription in conditional *spy sec* double mutants, suggesting both ACINUS-dependent and -independent mechanisms. These findings

provide a systematic framework for understanding the AS machinery in plants and uncovering how AS is regulated, paving the way for further exploration of AS mechanisms in plant systems.

Results

Profile ACINUS-associated alternative splicing-associated proteome using proximity-labeling and functional analysis

To gain a reliable and comprehensive understanding of the plant alternative splicing machinery, we sought to identify proteins associated with alternative splicing factors. As bait for TurboID-based proximity-labeling proteomic profiling (Fig.1a), we selected the evolutionarily conserved alternative splicing factor ACINUS, its paralog and interactor PININ, and its stable interactor SR45 (a homolog of RNPS1), all of which are known to regulate alternative splicing in both plants and animals(Fig. 1a)[13,33-35]. We fused ACINUS, PININ, and SR45 to TurboID-VENUS and expressed them under their native promoters in *acinus-2 pinin* double mutant or *sr45-1* mutant backgrounds (Fig. 1b). Control lines included TurboID fused to YFP in wild-type plants, as well as ACINUSΔRSB-TD (with a deletion of the 592-633 RSB domain)[36] to ensure specificity (Fig. 1b).

Confocal and spinning disk microscopy confirmed the nuclear localization of all three proteins (Fig. 1c, and Extended data Fig. 1a), with ACINUS being the most abundant and SR45 the least abundant. To confirm the physiological functionality of the fusion proteins, we evaluated leaf shape, rosette size, and flowering time in these lines. The *acinus pinin* and *sr45* mutants exhibit pleiotropic phenotypes, including narrow, twisted rosette leaves with serrated margins, small rosettes, and delayed flowering, with the *acinus pinin* mutants exhibiting a more severe phenotype. As expected, the full-length fusion constructs completely rescued these mutant phenotypes to wild-type levels (Fig.1d, Extended data Fig. 1b-c), confirming that the fusion proteins are functional in planta.

Comprehensive PL-MS mapping of the ACINUS-proxiome alternative splicing machinery with high confidence

We performed PL-MS on the ACINUS-TD, PNN-TD, and SR45-TD lines using protein-level enrichment for biotinylated proteins[37]. All three lines, along with their control lines, were treated with 50 μM biotin for 1 hour, with three biological replicates each. Biotinylated proteins were enriched using streptavidin beads, measured by LC/MS/MS, and quantified using label-free quantification (LFQ) (Fig.2a). Using a threshold of S0=2 and an FDR of 0.05 in Perseus, we identified 395, 324, and 255 proteins enriched by ACINUS-TD, PININ-TD, and SR45-TD, respectively (Fig. 2b-d), with known interactors (in red font) and novel interactors (in blue font) selectively labeled. The higher number of proteins enriched by ACINUS-TD is likely due to its higher expression, resulting in a higher signal-to-noise ratio, as indicated by the enrichment ratio difference shown on the x-axis, compared to PININ-TD and SR45-TD (Fig 2b-d). Therefore, we prioritized ACINUS for data integration.

Next, we used a complementary approach to directly detect and quantify biotinylated peptides enriched by ACINUS-TD using ^{15}N stable isotope labeling in Arabidopsis (SILIA) quantitative mass spectrometry[38]. ACINUS-TD and TD-YFP lines were metabolically labeled with ^{14}N and ^{15}N, respectively, and treated with 50 μM biotin for 1 h, followed by biotinylated peptide enrichment and ^{15}N quantification over four biological replicates (Fig. 2e). To ensure high confidence, the MS/MS peak lists were first filtered using the biotin signature ion (derivative ion at m/z 310.16 (^{14}N) or 311.16 (^{15}N) due to ammonia loss from the immonium ion of biotinylated lysine (ImKBio) (Extended Data Fig. 2a-2b), prior to subsequent search and quantification for biotinylated peptides (Extended Data Fig. 2c). Biotinylated peptides identified by both ^{14}N and ^{15}N labeling from ACINUS-TD-enriched samples were considered high confidence candidates. This analysis identified 156 significantly enriched proteins in the ACINUS-TD samples (Fig. 2f, Supplementary Table 1) that were quantified in at least three out of four replicates. While the peptide-level enrichment showed substantial overlap with the protein-level enrichment, it also uncovered unique biotinylated proteins, such as SERINE/ARGININE PROTEIN KINASE 5(SRPK5), providing complementary insights (Extended Data Fig 2, Supplementary Table 1).

To filter and integrate both data sets, we implemented a stringent filtering system to generate a confidence list (see Methods). We prioritized ACINUS-enriched proteins based on their overlap with enriched proteins by both PININ-TD and SR45 (n=171 proteins, including the three baits), exclusive overlap with PNN-TD (n=42) or SR45-TD (n=49), enrichment by ACINUS-TD at both protein and peptide level (n=15), and enrichment at the peptide level in at least 3 out of 4 replicates (n=21) (Fig.2g, Extended data Fig.3a, Supplementary Table 1). These stringent filtering steps result in a total network of 298 proteins. Notably, this high-confidence list includes 35 of the 47 proteins previously identified in our IP-MS using ACINUS as bait (Fig. 2g). Interestingly, 5 of the 12 missing proteins were significantly enriched by ACINUS-TD (Supplementary Table 1) but were omitted due to our stringent criteria. Overall, this integrated TurboID dataset significantly extends the identification of the ACINUS network.

To further assess the quality of our data set, we generated ACINUS-ΔRSB-TD transgenic lines with a deletion of the RSB domain 592-633 in the WT background. The truncated fusion protein was expressed at levels comparable to the full-length ACINUS-TD and localized to the nucleus (Fig. 1c). We compared the TurboID results of ACINUS-ΔRSB-TD to ACINUS-TD using protein-level enrichment and found that nearly 75% of the interactors showed either reduced or lost interactions (Fig.2h, Extended Data Fig.3b and 3c, Supplemental Table 1), This substantial loss of interactors underscores the reliability of the high confidence interaction list we identified (Fig. 2g). When ACINUS-ΔRSB-TD was transformed into the *acinus pnn* double mutant, the transgenic plants displayed the characteristic narrow, twisted rosette leaf phenotype observed in the double mutant. However, the transgenic plants were significantly larger than the double mutants (Extended Data Figs.3d-3e).

Interdependence of AS, transcription, and other mRNA processing steps

Gene Ontology (GO) term analysis based on biological function revealed that the ACINUS proxiome is significantly enriched for proteins involved in mRNA processing (Fig. 2i). These include a substantial number of homologs to known components of the spliceosome, as well as proteins associated with the regulation of gene expression, chromatin remodeling, non-coding RNA (ncRNA) processing, and ribonucleoprotein complex biogenesis. In addition, proteins associated with the vegetative to reproductive phase transition of the meristem were also enriched. These results are consistent with the established dual role of ACINUS in AS and transcription regulation.

To better understand the relationships between the identified interactors, we used Cytoscape to construct a comprehensive network[39]. Cytoscape facilitates the visualization and analysis of networks by allowing the integration of known and novel interactions. We imported protein interaction data from the STRING and GRID databases, where nodes represent proteins and edges represent their interactions. This allowed us to create a detailed map of these connections (Fig.3a) and organize the visualization based on their interactions and potential functional groups.

Many proteins within the network show strong connections, including 50 proteins with 3-9 edges (blue border) and 155 proteins with 10-109 edges (magenta border), representing known interactions (Fig.3a). We also identified a significant number of novel interactors: 37 proteins with minimal prior connections (1-2 edges, green border) and 56 proteins with no prior connections to the network (0 edges, yellow border). These novel interactors may have a role in mRNA processing, possibly analogous to that of ACINUS.

To test whether our ACINUS-proxiome supports the coupling between alternative splicing and transcription, we examined the interactomes (Supplemental Table 1). As expected, we detected many splicing factors with established or putative roles in splicing, including those integral to the NTC/PRP19 complex, which stabilizes the B complex and facilitates the transition from the B complex to the B^{act} complex (Fig.3a). We also identified factors involved in different stages of the splicing assembly and catalysis (A, B and B^{act}, and C complex) (Fig.3a). Furthermore, we identified core and accessory components of the spliceosome U1, U2, and U4/U6.U5 snRNP subunits, as well as Sm proteins (Fig.3a). Notably, we identified many key proteins involved in transcription and chromatin remodeling (Fig.3a), including three RNA polymerase II transcript elongation factors (TFIIS, TFIIE and TFIIEα,) and global transcription factors (GTA2, GTB1, GTE4). Components of the polymerase associated factor PAF1

complex were also detected (ELF5, ELF7, ELF8, VIP5)[40]. In addition, we identified chromatin remodeling factors or chromatin proteins (CHR5, CHR28, SWC4, SPT2), RNA polymerase II C-terminal domain phosphatases (CPL1, CPL3), SET domain proteins that regulate histone H3-K4 methylation (SDG2)[41], and RDR2-independent DNA methylation proteins (NERD). Our results provide strong evidence for interdependency between transcription and alternative splicing, supported by extensive mapping of the associated interaction.

To assess whether other RNA processing steps are closely linked to AS, we analyzed the proxiome and identified key proteins involved in various RNA processes such as 5' capping, m6A methylation, 3' polyadenylation, and mRNA export. For 5' capping, we detected the capping enzyme RNMT1, the capping binding protein complex (CBP20 and CBP80), the associated protein SE, and the decapping proteins XRN3 and DXO1. In particular, DXO1 has recently been reported to associate with and activate RNMT1 for m7G capping[42]. For m6A methylation, we identified the mRNA adenosine methylases MTA and MTB, as well as components of the m6A writer complex HIZ1 and HIZ2. For 3' polyadenylation, our analysis revealed key players, including the cleavage and polyadenylation specificity factors CPSF30, CPSF6/7A and CPSF6/7B, the polyadenylation factor protein PCFS4, and the poly(A) polymerase interactor FIP1. We also identified several proteins with putative roles in mRNA transport, including ALY1, ALY2, ALY3, ALY4 and THO1, THO2, THO5B and UAP56A, all of which are components of the TREX complex. Taken together, our results provide compelling evidence that these processes are highly connected, potentially facilitating efficient mRNA processing.

ACINUS-proxiome reveals high redundancy

To examine features and redundancy of the ACINUS-proxiome, we analyzed the network using Interpro, which classifies proteins into families and predicts domains. This analysis revealed a significant enrichment of features associated with AS, including RNA binding domain (RBD), helicase, zinc finger motifs (Znf_CCHC, Znf_CCCH, Znf_RING/FYVE/PHD), WD40, G-patch, kinase, WW, and SURP motif (Fig. 3b, Supplemental Table 1). Remarkably, the network shows extensive redundancy, with 21 helicases, 7 cyclophilin-type PPIases, 7 WD-40 containing proteins, and 6 kinases (Fig. 3b). The identified kinases include members of the SRPK family group II (SRPK4, SRPK5), the LAMMER kinase family (AFC1), CLK kinases (CDKG1 and CDKG2), and a splicing kinase (PRP4KA). These plant kinases share homology with human counterparts that have been implicated in the regulation of AS[43]. The redundancy underscores the complexity of the AS regulatory system in plants, paralleling the intricate splicing machinery observed in animal systems.

Shared and distinct AS events regulated by different components in the network

We hypothesized that depletion of the proteins identified with the same network would result in similar or opposite phenotypic changes - either in the molecular phenotype, such as AS events, or in the morphological phenotype - compared to the *acinus pinin* double mutant. To test this hypothesis, we first analyzed AS events in several mutants with available RNA-seq data (*skip, mac3mac3b, prp18a, prp4ka, luc7a luc7b luc7rl, xrn3,* and *sac3a*)[44-48]. We then evaluated the morphological phenotype in mutants of selected interactors (*tgh-1*, *dxo-1*)[42,49].

Both SKIP and MAC3A/MAC3B belong to the NTC (Nineteen complex), which is essential for the proper assembly and activation of the spliceosome[44]. PRP18A is involved in the second step of pre-mRNA splicing[45], while PRP4KA is a serine/threonine kinase that is part of the spliceosome machinery[47]. The LUC homologs are part of the U1 snRNP[48], and XRN3 encodes a 5' to 3' exoribonuclease[46]. SAC3A, a putative mRNA export factor, is highly co-expressed with PRP4KA[47]; however, its precise role in mRNA export remains to be elucidated[50].

To improve data analysis, we improved both the sequencing of our *acinus pinin* mutants and the methods used to detect intron retention. We performed new paired-end (150bp) non-stranded sequencing for both WT and *acinus pinin* mutants, achieving an average of 57.2 million reads per replicate. This improved data greatly enhances the detection of fragments spanning exon-exon and exon-intron junctions, which is critical for accurate AS analysis[51]. This is a significant improvement over our previous sequencing,

which averaged 22.4 million single end (100bp) reads[52]. In addition, we refined our intron retention detection method by introducing the intron read depth ratio calculation (IDratio, Extended data Fig. 4a) into RackJ. The IDratio quantifies cDNA with retained introns relative to the total cDNA for a given gene, based on the read depth of the intron and its flanking exons. This metric provides a more intuitive measure of intron retention than our previous intron coverage ratio; for example, an IDratio of 0.1 indicates that 10% of transcripts for a given gene have retained introns.

Using this improved detection method and several filtering steps (Extended data Fig. 4a), we obtained a total of 1010 altered intron retention events (839 increased in 688 genes and 171 decreased in 156 genes) in the *acinus pinin* mutant. Re-analysis of the RNA-seq results for the *skip, mac3a mac3b, prp18a, prp4ka, luc7a luc7b luc7rl, xrn3, and sac3a* mutants revealed strikingly common targets with the *acinus pinin* mutant, with *skip* showing the most overlapping events, and *xrn3* showing the fewest (Fig.4a-g, Extended data Fig.4b). Splicing factors can have both positive and negative effects on AS in a context-dependent manner. In our analysis, we found that most of the regulated events showed the same directionality, indicating that the knockout of these components primarily leads to increased intron retention (Fig.4h). Notably, although SAC3A was identified in a splicing reporter screen and annotated as a putative mRNA export factor, neither STRING nor GRID showed any associations with other splicing factors (Fig.3a). Our proteomic data suggest that SAC3A is part of the ACINUS network, which is further supported by the AS analysis that approximately ¼ of the intron retention events detected in the *sac3a* mutants were also found in the *acinus pinin* mutants.

To test whether other components of the network have a morphological phenotype similar to the *acinus pinnin* double mutant, we examined the mutant phenotype of TGH and DXO1. TOUGH (TGH) interacts with TATA-box binding protein 2 and colocalizes with the splicing regulator SR34 to subnuclear particles[49], while DXO encodes a NAD-RNA decapping enzyme that activates RNMT1 to methylate the guanosine cap of mRNA[42,53]. The comparison revealed that both mutants exhibited reduced plant size and narrow, often pointed and curled leaves, mirroring the phenotypes observed in the *acinus pinin* mutants, albeit to a lesser extent. Furthermore, *dxo1-1* displayed a pale green phenotype similar to that of the *acinus pinin* mutants (Fig 4i).

SPY and SEC regulate alternative splicing and transcription via ACINUS-dependent and -independent way

Among the ACINUS network proteins, 47 were previously identified as O-GlcNAcylated, 30 were O-fucosylated, and 20 were doubly modified (Fig. 5a)[28-30], including ACINUS, HRLP, PRP16, SUA, CPL3 (Fig. 5b). We hypothesize that SPY and SEC may regulate gene expression via AS and/or transcription, both in an ACINUS-dependent and -independent manner. Previous qPCR analyses in *spy* and *sec* single mutants revealed splicing defects in several genes that are also affected in *acinus pinin* mutants[13]. Therefore, we investigated both single and double mutants to further understand these regulatory roles.

To elucidate the role of SPY and SEC in AS masked by embryonic lethality [29,54], we generated a conditional double mutant by introducing short hairpin *SEC RNAi* into a *spy-4* null background (termed as *shSECi*) (Extended data Fig.5a). On control plates, this line resembled *spy-4* with short roots, but on plates containing dexamethasone (Dex), they exhibited early seedling lethality (Extended data Fig. 5b). When *shSEC RNAi spy-4* seedlings were transferred from normal plates to plates containing Dex-containing plates, they showed progressively reduced root growth by day 3, leaf discoloration by day 5, and complete growth arrest by day 7 (Fig.5c and Extended data Fig. 5c-5d). These phenotypes are similar to, but more severe than, those observed in the *a2 SEC RNAi spy-3* inducible line[55] (Fig. 5c and Extended data Fig. 5b-5d).

We performed a genome-wide comparison of AS and transcription in WT, *spy-4*, *acinus pnn*, and *shSECi* lines (see Methods). A *sec* single mutant was excluded due to the lack of phenotype, which is likely compensated by SPY[56]. To assess data quality and to evaluate the potential effects of DMSO treatment, we performed a principal component analysis (PCA) on the transcriptomic data. The PCA results confirmed that replicates from WT, *acinus pinin,* and Dex treated *shSECi* clustered closely together, and that their biological groupings are distinct (Extended data Fig. 6a). The biological groupings of DMSO treated

shSECi and *spy-4* lines clustered closely together, which indicates that DMSO has minimal transcriptional effects on seedlings. A total of 1,155 up- or down-regulated transcripts were shared between *acinus pnn* and Dex treated *shSECi* seedlings ($\log_2$FC $\geq$ 2 and FDR$\leq$ 0.05), accounting for 66.3% of *acinus pnn*-dependent and 18.6% of *shSECi* (+Dex)-dependent events, when compared to WT (Fig.5 d and e, Extended data Fig. 6b).

Next, we analyzed the intron retention changes shared by the *acinus pnn* and *shSEC RNAi spy-4* (+Dex) mutants. Remarkably, 141 IR events were common to both mutants, accounting for 13.9% of *acinus pnn*-dependent events and 27.1% of *spy sec*-dependent events (Fig. 5f-g). Co-dependent splicing events tended to be similarly altered in *acinus pnn* and *shSEC RNAi spy-4* (+Dex), with either increased or decreased intron retention (Fig.5h). Comparable results were also observed in the *spy-4* mutant and *shSEC RNAi spy-4* (+ mock) (Fig.5h), with the latter showing surprisingly more increased intron retention events. In contrast, a comparison with the *skip* mutant revealed a significant overlap of events, but mainly for increased intron retention (Fig. 5i); SKIP has previously been shown to be O-GlcNAc modified (Fig 5b). These common and distinct IR and transcription events suggest that SPY and SEC regulate AS and transcription in both an ACINUS-dependent and -independent manner, highlighting the complexity of plant regulatory systems.

Discussion

By integrating label-free quantification and SILIA with TurboID-based LC-MS/MS data enriched at both the protein- and peptide-level, we have generated for the first time a comprehensive map of the ACINUS-centered network controlling AS. Validation of the newly identified ACINUS proximal partners by RNA-seq analysis of AS events as well as phenotypic analysis highlights the robustness of our methodology. These results reveal a strong link between AS, transcription and chromatin remodeling, as well as interdependencies with other mRNA processing steps (Fig.6a). Furthermore, we show that SPY and SEC regulate AS and transcription through ACINUS-dependent and -independent pathways (Fig.6b).

Numerous efforts have been made to map the repertoire of proteins involved in AS, using different proteomic approaches, such as IP-MS using either splicing factors or unspliced mRNA as bait, as well as genetic strategies such as systematic RNAi or CRISPR-Cas-mediated gene ablation, as reviewed by Ule and Bencowe[19]. Our TurboID-based analysis provides an exceptionally sensitive approach to identify both known and novel components associated with ACINUS-mediated complexes involved in AS. By applying rigorous criteria during data analysis, we ensured high confidence identification of 298 components, although the possibility of some false negatives remains. For example, while certain interactors previously identified by IP-MS were enriched by our TurboID baits, they were excluded by these stringent filters. Despite these limitations, our approach provides a robust and reliable map of the ACINUS interactome, allowing a comprehensive and confident assessment of plant proteins involved in AS.

Our data reveals a significant redundancy of the proteins detected in the ACINUS interactome, including many protein families previously implicated in AS, such as SR proteins, hnRNPs, RNA-binding proteins, K homology domain proteins, and zinc finger proteins. This finding is consistent with the biochemical and cryo-electron microscopy studies showing that eukaryotic spliceosomes, such as the human spliceosome, contain more regulatory components and are significantly more dynamic than the yeast spliceosome[57,58]. The observed redundancy highlights the complexity of the AS regulatory systems in plants, mirroring the functional plasticity and complexity of the animal splicing machinery. This plasticity likely allows plants to fine-tune mRNA processing in responses to different physiological and environmental contexts, as AS, particularly intron retention, has been shown to be induced in response to environmental cues.

Our InterPro feature analysis highlights conserved mechanisms between plants and animals, as evidenced by the identification of many human counterparts within the ACINUS interactome by BLAST analysis (Supplemental Table 1). These common components suggest a broadly conserved AS machinery across eukaryotes. However, the presence of poteins with no detectable human homologs, including those lacking InterPro domains (n=12) and those with plant-specific domains (n=9) (Supplemental Table 1),

underscores the unique adaptation of the plant splicing machinery. These plant-specific features raise the intriguing question of how intron definition remains the dominant form of AS in plants, despite the apparent similarities in the composition of the AS machinery compared to that of animals. This highlights the need for further investigation of the evolutionary and functional divergence of splicing regulations in plants.

Notably, while many proteins have many connections in the network, as determined by STRING and GRID, their precise biochemical and biological roles remain to be fully elucidated. On the other hand, multiple novel interactors with no prior connection were identified. For instance, SAC3A, which was previously identified in a genetic screen and confirmed by RNA-seq in the role of AS[47], lacks connection to AS in our STRING analysis, displays remarkably overlapping intron retention patterns - approximately 25% shared with the *acinus pinin* mutants. Future genetic, biochemical studies, and structural analysis are needed to further elucidate the functions of these proteins in AS and to uncover the mechanistic underpinning of their roles in RNA processing.

Interdependent mRNA processing has been demonstrated in mammals[59] and in plants[60], with evidence showing that the RNAPII C-terminal domain recruits splicing factors to nascent mRNAs. Long reads sequencing nascent RNA chains further supports this coupling, which tightly integrates AS with transcription. Consequently, AS is influenced by transcriptional kinetics and chromatin structure, and vice visa. Our proteomic data, using ACINUS, PININ and SR45 as baits, identified numerous proteins involved in transcription and chromatin remodeling factors (Fig. 3a), supporting the co-transcriptional nature of AS. We also detect proteins involved in capping, m6A methylation, 3' cleavage and polyadenylation, and mRNA export, further suggesting that these processes are associated with AS (Fig. 6a). Notably, the supraspliceosome hypothesis proposes that mRNA processing steps occur in phase-separated condensates that coordinate the numerous processing steps and facilitate efficient mRNA processing[19,61-63]. Our results suggest that a similar mechanism of coordinated mRNA processing exists in plants.

Our RNA-seq data shows that SPY and SEC regulate over 7000 gene expression and over 500 intron retention events. To distinguish between direct and indirect effects, we performed RNA-seq analysis 3 days after Dex treatment, a time point when the conditional double mutants have detectable RNAi expression and are just beginning to show phenotype. At this early stage, it is possible that SEC is not fully inhibited, leaving residual SEC activity that could influence the observed molecular phenotype. Endogenous SEC expression is hard to detect by mass spectrometry[64], making the quantitative analysis of SEC protein expression in the conditional double mutant difficult. Nevertheless, the clear pattern of intron retention provides strong evidence that SPY and SEC regulate alternative splicing and transcription through both ACINUS-dependent and -independent pathways. We also surprisingly observed more increased intron retention in DMSO-treated plants, while transcriptional analysis shows that they are similar to *spy-4* single mutants, it is possible that there is some leaky expression, and that SPY and SEC have opposite and overlapping roles[65,66]. Our study shows that sugar modifications have profound effects on AS and transcription. In the future, it would be interesting to understand how exactly sugar modifications affect the splicing machinery to influence functions.

Acknowledgement

We thank Dr. Laila Moubayidin lab at John Innes Center for sharing the a2 SECamiRNAi line, Dr. Xiao-Ning Zhang at St Bonaventure University for sharing *sr45-1* mutant seeds, and Dr. Andrea Mair and Dr. Dominique Bergmann at Stanford University for providing the TurboID gateway clones. We also thank the Arabidopsis Biological Resource Center (ABRC) for providing several mutant seed stocks and to William Conner for photographing mutant phenotypes. This work is supported by the National Institutes of Health (R01GM135706 and S10OD030441to S.-L.X., and diversity supplement to A.V.R.; and R01GM066258 to Z.-Y,W), Carnegie Endowment Fund to the Carnegie Mass Spectrometry Facility.

Contribution

R.S, D.B, A.V.R and S.K.R. generated TurboID constructs and transgenic lines. R.S. carried out TurboID experiments. A.V.R performed data mining and refined the IR analysis pipeline with assistance from W.D.L. S.K.R generated and characterized *shSECi* lines in *spy-4* and *spy-3* line under supervision by S.L.X

and Z.Y.W. S.C. and S.K.R generated RNA-Seq data and S.C. and A.V.R analyzed the RNA-seq data. J.L. and H.C. generated shSECi construct. S.K.R and K.A. performed microscopy, W.Z. characterized truncated construct phenotype. S.L.X. conceived the projects and wrote the manuscript.

Data Availability

The mass spectrometry proteomics data have been deposited to the ProteomeXchange Consortium via the PRIDE partner repository with the dataset identifiers. The RNA-seq data have been deposited at NCBI Gene Expression Omnibus (GEO) database under the access number. All other data is available from the corresponding author on reasonable request.

Methods and materials

Plant materials and growth conditions

All Arabidopsis plants used in this study were in the Columbia-0 (Col-0) background. The *tgh-1* mutant (SALK_053445) and the *dxo1* mutant (SALK_103157) were obtained from the Arabidopsis Biological Resource Center (ABRC). For seedlings grown on the medium in petri dishes, all the sterilized seeds were stratified at 4°C for 2-3 days and grown on the specified medium for the time indicated in each experiment.

For plants grown in the greenhouse, a 16-h light/8-h dark cycle at 22–24 °C was used for general growth or photo collection, as described in each experiment. Most of the seedlings were grown vertically on ½ Murashige and Skoog medium and supplemented with 0.8% (w/v) phytoagar under constant light (24 h light, 22°C) for the time indicated in each experiment. For protein-level enrichment of biotinylated proteins using label-free quantification (LFQ), seedlings were harvested after 10 d and treated with biotin at 50 μM for 1 h. For peptide-level enrichment of biotinylated proteins using SILIA, the bait and control lines were grown at 22°C on ^{14}N or ^{15}N medium plates (Hogland's No2 salt mixture without nitrogen 1.34g/L, 6g/L phytoblend, and 1g/L KNO_3 or 1g/L $K^{15}NO_3$ (Cambridge Isotope Laboratories) for ^{14}N medium or ^{15}N medium, respectively, pH5.8) for 14 days and then treated with 50 μM biotin for 1h. For RNA-seq, wild-type (WT), *acinus pinin*, *spy-4* were grown on ½ MS for 8 days before harvesting. *shSEC RNAi spy-4* were grown on ½ MS plates were grown on ½ MS for 5 days and transferred to mock or Dex treated plates for 3 days before harvesting.

Construct generation and transformation

The full-length cDNA of ACINUS, PININ and SR45, and the truncated cDNA of ACINUSΔRSB were cloned into pENTRD-TOPO vectors. The promoters, approximately 2 kb upstream of the ATG start codon of ACINUS, PININ and SR45, were amplified and cloned into the pENTR5 vector gateway clone to generate the promoter entry clone (pENTR5-ACINUSpro, or PININpro, or SR45pro). The ACINUS-TD, PNN-TD, SR45-TD, and ACINUSΔRSB-TD constructs were generated by multisite gateway cloning, allowing LR reactions of three entry vectors (the promoter entry clone, the cDNA entry clone, and pDONR_P2R-P3_R2-Turbo-mVenus -STOP-L3) with the destination vector pB7m34GW [37] to generate the final expression vector. The control constructs TD-YFP under three different promoters were generated by multisite gateway cloning, allowing LR reactions of two entry vectors (the promoter entry clone, pENTR_L1-Turbo-YFP-NLS-STOP-L2) with the destination vector R4pGWB501 to generate the final expression vector. Related primers are listed in Supplemental Table 2.

ACINUS-TD, PININ-TD were transformed into the *acinus-2 pinin* mutants, SR45-TD was transformed into the *sr45-1* mutants. ACINUSΔRSB was transformed into WT for TurboID experiments, and into *acinus-2 pinin* mutants for phenotypic analysis. These lines were selected using BASTA. The various TD-YFP controls were transformed into wild-type and selected on hygromycin. Complemented bait-TD lines and TD-YFP lines were selected for their expression level or complementation phenotype or both. T3 lines were used for phenotypic analysis and TurboID experiments.

shSEC RNAi lines: The short hairpin SEC RNA (*shSEC RNAi*) constructs for *SEC* were made by linking two fragments PCR-amplified from the 5' end of the genes (genomic DNA or gDNA, 34-846 relative to ATG start site) and cDNA (34-389 relative to ATG start site) in an head-to-head orientation,

with primers specified in primer table (SEC_gDNAF/SEC_R to amplify genomic DNA; SEC_cDNA_F/SEC-R to amplify cDNA). XhoI or PstI site was added to the 5' end of the primers used for cloning. The inverted constructs were first cloned in pBluescript II SK+ and then subcloned into the XhoI and SpeI sites in the Dex-inducible binary vector pTA7002[67]. The construct was transformed into the *spy-3* and *spy-4* mutant. Over 100 T2 independent lines in the *spy-3* were screened, with 2 lines showing reduced root phenotype. In the *spy-4* background upon Dex treatment, a total of 14 independent lines were screened, and 4 lines showed a strong growth arrest phenotype in the presence of Dex treatment. These T3 homozygous lines were used for phenotypic analysis and RNA-seq.

Functional analysis of bait-TD fusion complementation analysis

The following lines were sterilized and grown on ½ MS plates under constant light for 10 days: WT, *acinus-2 pinin*, *sr45-1* mutant, ACINUS-TD/*ap*, PININ-TbID/*ap*, SR45-TbID/*sr45-1*, then transplanted to soil and grown under long day conditions (L/D of 16h/8h) at 22ºC. Photos were taken of plants at approximately 3 weeks old and 5 weeks old to compare leaf size and shape, and flowering time. Similarly, *acinus-2 pinin,* ACINUSΔRSB-TD/*ap* were grown on ½ MS plates under constant light for 7 days then transplanted to soil and grown under long day conditions (L/D of 16h/8h) at 22ºC. Photos were taken at plants of approximately 3 weeks old to compare leaf size and shape.

Confocal Microscopy and Spinning disk Microscopy

Images of 4-day-old Arabidopsis seedlings expressing BAIT-TurboID (which also contains VENUS) constructs were taken with a Leica SP8 confocal microscope and spinning disk microscope. Images were processed using Adobe photoshop and ImageJ software.

Root length quantification assay

Wild-type (WT), *spy-4*, *shSEC RNAi spy-4*, and *a2SEC RNAi spy-3* seeds were grown on ½ MS medium supplemented with 10 µM Dex or DMSO. After 10 days, the seedlings were photographed for phenotypic analysis to assess their response to Dex treatment. Alternatively, seeds were grown on ½ MS plates for 5 days before being transferred to ½ MS medium containing either 10 µM Dex or DMSO mock treatment. Seedlings were imaged at 0-, 3-, 5-, and 7-days post-transfer, and root elongation was measured using ImageJ software. Over 15 seedlings per sample were measured.

Biotinylated protein enrichment at protein-level and peptide-level

Tissue samples (1 g each) were harvested in triplicate per condition. Biotinylated proteins were enriched at the protein-level using MyOne Streptavidin C1 Dynabeads (Invitrogen) with steps described in[37]. The ACINUS-TurboID experiments included WT, ACINUS-TD, ACINUSΔRSB-TD/WT, and TD-YFP. The PNN-TurboID experiments included PNN-TD and a corresponding TD-YFP control, while the SR45-TurboID included SR45-TD and its TD-YFP control.

For peptide-level enrichment, ~ 2 g of tissue was harvested per sample, with 4 biological replicates (two ^{14}N-labeled and two ^{15}N labeled) for both bait and control, Tissues were equally mixed as the following: Fw1: ^{14}N ACINUS-TD /^{15}N YFP-TD; Rv1, ^{15}N ACINUS-TD/ ^{14}N YFP-TD; Fw2: ^{14}N ACINUS-TD /^{15}N YFP-TD; Rv2:^{15}N ACINUS-TD/ ^{14}N YFP-TD. Proteins were extracted from mixed tissues using phenol extraction, digested and cleaned as described as[28]. The peptide mixture was resuspended in the PBS buffer and incubated with 100 µL of Dynabeads M-280 Streptavidin (Thermo, 11206D) prewashed in the PBS buffer. The resulting mixture was incubated for 1 h at room temperature with shaking at 800 rpm. The beads were washed first with PBS twice, then with PBS with 5% ACN twice and finally with ddH_2O once, each for 5 min at room temperature and 800 rpm. The biotinylated peptides were eluted with 200 µL of elution buffer (0.2% TFA, 0.1% FA, and 80% ACN) three times by heating at 75ºC for 5 min. The eluted peptides were collected and dried by speedvac. The peptide mixtures were desalted using C18 OMIX Tips.

LC-MS/MS analysis

Peptides were analyzed by liquid chromatography–tandem mass spectrometry (LC-MS) on an EasyLC1200 system (Thermo) connected to a high-performance quadrupole Orbitrap Q Exactive (Thermo), with parameters as described[37]. Biotinylated peptides were eluted with a slight modification: from 3 to 6% solvent B (80% (v/v) acetonitrile/0.1% (v/v) formic acid) over 1 min, 6-10% solvent B over 4 min, 10 to 45% solvent B over 96 min, from 45 to 75% solvent B over 20 min, followed by a short wash of 8 min by 90% solvent B.

Label-free Quantification for Protein-level enrichment and statistics processing using Perseus

Raw MS/MS data was loaded in Maxquant (v2.4.12). The search was using most of the preconfigured settings allowing match between runs options. Data was searched with a 4.5 ppm tolerance for precursor ions and 20 ppm for fragment ions. Peptide and protein FDRs were set as 0.01. Label-free quantification (LFQ) was enabled. Data was searched against the TAIR10 database *Arabidopsis thaliana* (https://www.arabidopsis.org/), concatenated with decoy protein sequences (a total of 35386 entries). A Maxquant LFQ was run with min ratio count as 2 (a minimum of 2 peptides quantification per protein) was required and match time window with 0.7 min, Quantification was done on unique and razor peptides and other parameters as default. Match between runs was applied. The data were filtered as described[37]. A two-sided T-test with S0=2 and FDR=0.05 was used to determine significance and enrichment of protein.

SILIA quantification for peptide-level enrichment using Protein Prospector

For Protein Prospector (version 6.4.9), MS/MS data were converted into peaklists using the script PAVA (peaklist generator that provides centroid MS2 peaklist). The peaklists were further filtered using signature ion peak 310.16 or 311.16 to generate filtered peaklists. Both full and filtered peaklists were searched using the same parameters, the former to confirm equal mixture of ^{14}N- and ^{15}N-labeled peptides and the latter to identify and quantify biotinylated peptides. A precursor mass tolerance of 10 ppm and MS/MS2 tolerance of 20 ppm were allowed. Carbamidomethyl (cysteine (C)) was searched for as a constant modification. Variable modifications allowed included biotinylation at uncleaved lysines (Biotin(K)), protein N-terminal acetylation, methionine (M) oxidation, N-terminal acetylation with M oxidation, N-terminal M-loss, N-terminal M-loss with acetylation, and peptide N-terminal Gln conversion to pyroglutamate, with three maximum variable modifications per peptide. Similar ^{15}N parameters were used for ^{15}N samples. Cleavage specificity was set to trypsin, allowing two missed cleavages. For Protein Prospector, default 1% FDR was allowed for peptides and 5% for proteins. The quantification was done as described in Shrestha et al.[38, 29] but reporting on both protein-level (medium ratio of quantified peptides from the same protein) and peptide-level (ratio of each peptide from the same protein). As ^{14}N and ^{15}N labeled peptides have different masses in both MS1 and MS2, peptides identified by both are of high confidence.

Data integration and filtering

The data were rigorously filtered to generate a robust ACINUS-proxiome list (see Supplementary Table 1). The 1st category included 171 proteins (including three baits) that were enriched for all three baits: PNN-TD (protein-level) and SR45-TD (protein-level), and ACINUS-TD (protein-level or peptide-level). The 2nd included 42 proteins enriched by PNN-TD (protein-level) and ACINUS-TD (protein-level or peptide level). The 3rd category included 49 proteins enriched by SR45-TD (protein-level) and ACINUS-TD (protein-level or peptide-level). The 4th category identified 15 proteins that were enriched by ACINUS-TD (both protein-level and peptide level). The 5th included 21 proteins that are exclusively enriched by ACINUS-TD at the peptide level (in at least 3 reciprocally labeled experiments, ≥10 fold cut off).

RNA Seq analysis and data mining

Paired-end RNA-seq data for WT, *spy-4*, *shSEC RNAi spy-4* (mock and Dex treated) samples were generated using the Illumina platform NovaSeq X Plus Series (PE150) at Novogene (California). Raw reads were trimmed using CutAdapt (Version 2.6), quality checked using fastqc (Version X) and aligned to the genome using STAR (Version 2.7.10b). STAR alignment was done with araport11 annotation (Araport11_GFF3_genes_transposons.Jan2024 and Araport11_GTF_genes_transposons.Jan2024) and TAIR10 genome sequence downloaded from arabidopsis.org. Alignment files were processed using

RACKJ (Version 0.99a) to retrieve both read counts and read depth for each annotated intron and exon. For intron retention analysis the intron read depth ratio (IDratio) was calculated by dividing the intron read depth of the given intron by the average read depth of the two flanking exons. However, for the first and last intron the IDratio is calculated using the depth of the second (3') or first (5') flanking exon, respectively, because read depths for the first and the last exon in a gene may be inaccurate due to sequencing bias. Undefined IDratios (e.g., when divided by zero) were imputed using a normal distribution downshifted by 1.8 standard deviations and a mean reduction by a factor of 0.3. All IDratios were $\log_2$ transformed prior to significance calculation ($\alpha < 0.05$) in order to determine which introns were significantly increased in the *acinus pnn* double mutant. A two-tailed t-test was performed on both WT and mutant replicates (n =4). Introns were filtered using the following criteria: (1) p-value less than 0.05; (2) fold change less than 1.5; (3) belonging to a gene with an average RPKM less than 1; (4) average intron depth less than 5; (5) not belonging to single intron genes; (6) mean IDratiomut less than 0.15. Similar steps were performed in the *acinus pinin* mutant to determine intron reduction.

For expression analysis, ReadsPerGene files from the STAR alignment were processed in R using Deseq2. The lfcShrink function was applied as described[68]. Genes were defined as significantly differentially expressed if they had an adjusted p-value less than or equal to 0.05 and a fold change of less than or equal to 2. For all heatmaps, normalized gene counts were $\log_2$ transformed. All non-numerical values (e.g., -Inf) were imputed using the method described above. For PCA analysis, genes containing -Inf Values were removed.

For data mining, relevant RNA-seq data files were downloaded using NCBI sra-tool's fasterq-dump (2.11.2) (Supplemental Table 3). The downloaded RNA-seq data was checked for quality using fastqc and subsequently processed by STAR aligner using the method described above. STAR parameters were adjusted for unpaired and/or shorter read lengths accordingly. Statistical significance for Venn diagram overlap was generated using a hypergeometric test in R. The analysis results were detailed in Supplemental Table 3.

Reference

1 Kornblihtt, A. R. *et al.* Alternative splicing: a pivotal step between eukaryotic transcription and translation. *Nat Rev Mol Cell Biol* **14**, 153-165, doi:10.1038/nrm3525 (2013).

2 Nilsen, T. W. & Graveley, B. R. Expansion of the eukaryotic proteome by alternative splicing. *Nature* **463**, 457-463, doi:10.1038/nature08909 (2010).

3 Pan, Q., Shai, O., Lee, L. J., Frey, B. J. & Blencowe, B. J. Deep surveying of alternative splicing complexity in the human transcriptome by high-throughput sequencing. *Nat Genet* **40**, 1413-1415, doi:10.1038/ng.259 (2008).

4 Chaudhary, S. *et al.* Alternative Splicing and Protein Diversity: Plants Versus Animals. *Front Plant Sci* **10**, 708, doi:10.3389/fpls.2019.00708 (2019).

5 Chaudhary, S., Jabre, I., Reddy, A. S. N., Staiger, D. & Syed, N. H. Perspective on Alternative Splicing and Proteome Complexity in Plants. *Trends Plant Sci* **24**, 496-506, doi:10.1016/j.tplants.2019.02.006 (2019).

6 Salz, H. K. Sex determination in insects: a binary decision based on alternative splicing. *Curr Opin Genet Dev* **21**, 395-400, doi:10.1016/j.gde.2011.03.001 (2011).

7 Dillman, A. A. *et al.* mRNA expression, splicing and editing in the embryonic and adult mouse cerebral cortex. *Nat Neurosci* **16**, 499-506, doi:10.1038/nn.3332 (2013).

8 Baralle, F. E. & Giudice, J. Alternative splicing as a regulator of development and tissue identity. *Nat Rev Mol Cell Biol* **18**, 437-451, doi:10.1038/nrm.2017.27 (2017).

9 Scotti, M. M. & Swanson, M. S. RNA mis-splicing in disease. *Nat Rev Genet* **17**, 19-32, doi:10.1038/nrg.2015.3 (2016).

10 Bonnal, S. C., Lopez-Oreja, I. & Valcarcel, J. Roles and mechanisms of alternative splicing in cancer - implications for care. *Nat Rev Clin Oncol* **17**, 457-474, doi:10.1038/s41571-020-0350-x (2020).

11 Bradley, R. K. & Anczukow, O. RNA splicing dysregulation and the hallmarks of cancer. *Nat Rev Cancer* **23**, 135-155, doi:10.1038/s41568-022-00541-7 (2023).
12 Jia, J. *et al.* Post-transcriptional splicing of nascent RNA contributes to widespread intron retention in plants. *Nat Plants* **6**, 780-788, doi:10.1038/s41477-020-0688-1 (2020).
13 Bi, Y. *et al.* Arabidopsis ACINUS is O-glycosylated and regulates transcription and alternative splicing of regulators of reproductive transitions. *Nat Commun* **12**, 945, doi:10.1038/s41467-021-20929-7 (2021).
14 Yan, Y. *et al.* Light controls mesophyll-specific post-transcriptional splicing of photoregulatory genes by AtPRMT5. *Proc Natl Acad Sci U S A* **121**, e2317408121, doi:10.1073/pnas.2317408121 (2024).
15 Godinho, D. P., Yanez, R. J. R. & Duque, P. Pathogen-responsive alternative splicing in plant immunity. *Trends Plant Sci*, doi:10.1016/j.tplants.2024.11.010 (2024).
16 Keren, H., Lev-Maor, G. & Ast, G. Alternative splicing and evolution: diversification, exon definition and function. *Nat Rev Genet* **11**, 345-355, doi:10.1038/nrg2776 (2010).
17 Han, H. *et al.* Multilayered Control of Alternative Splicing Regulatory Networks by Transcription Factors. *Mol Cell* **65**, 539-553 e537, doi:10.1016/j.molcel.2017.01.011 (2017).
18 Gonatopoulos-Pournatzis, T. *et al.* Genome-wide CRISPR-Cas9 Interrogation of Splicing Networks Reveals a Mechanism for Recognition of Autism-Misregulated Neuronal Microexons. *Mol Cell* **72**, 510-524 e512, doi:10.1016/j.molcel.2018.10.008 (2018).
19 Ule, J. & Blencowe, B. J. Alternative Splicing Regulatory Networks: Functions, Mechanisms, and Evolution. *Mol Cell* **76**, 329-345, doi:10.1016/j.molcel.2019.09.017 (2019).
20 Barbosa-Morais, N. L. *et al.* The evolutionary landscape of alternative splicing in vertebrate species. *Science* **338**, 1587-1593, doi:10.1126/science.1230612 (2012).
21 Fica, S. M., Oubridge, C., Wilkinson, M. E., Newman, A. J. & Nagai, K. A human postcatalytic spliceosome structure reveals essential roles of metazoan factors for exon ligation. *Science* **363**, 710-714, doi:10.1126/science.aaw5569 (2019).
22 Arabidopsis Genome, I. Analysis of the genome sequence of the flowering plant Arabidopsis thaliana. *Nature* **408**, 796-815, doi:10.1038/35048692 (2000).
23 Zhu, L. *et al.* Patterns of exon-intron architecture variation of genes in eukaryotic genomes. *BMC Genomics* **10**, 47, doi:10.1186/1471-2164-10-47 (2009).
24 Grau-Bove, X., Ruiz-Trillo, I. & Irimia, M. Origin of exon skipping-rich transcriptomes in animals driven by evolution of gene architecture. *Genome Biol* **19**, 135, doi:10.1186/s13059-018-1499-9 (2018).
25 Petrillo, E. Do not panic: An intron-centric guide to alternative splicing. *Plant Cell* **35**, 1752-1761, doi:10.1093/plcell/koad009 (2023).
26 Chen, M. & Manley, J. L. Mechanisms of alternative splicing regulation: insights from molecular and genomics approaches. *Nat Rev Mol Cell Biol* **10**, 741-754, doi:10.1038/nrm2777 (2009).
27 Kretova, M., Selicky, T., Cipakova, I. & Cipak, L. Regulation of Pre-mRNA Splicing: Indispensable Role of Post-Translational Modifications of Splicing Factors. *Life (Basel)* **13**, doi:10.3390/life13030604 (2023).
28 Xu, S.-L. *et al.* Proteomic analysis reveals O-GlcNAc modification on proteins with key regulatory functions in Arabidopsis. *Proc. Natl. Acad. Sci. U. S. A.* **114**, E1536-E1543, doi:10.1073/pnas.1610452114 (2017).
29 Shrestha, R., Karunadasa, S., Grismer, T., Reyes, A. V. & Xu, S. L. SECRET AGENT O-GlcNAcylates hundreds of proteins involved in diverse cellular processes in Arabidopsis. *Mol Cell Proteomics*, 100732, doi:10.1016/j.mcpro.2024.100732 (2024).

30 Bi, Y. *et al.* SPINDLY mediates O-fucosylation of hundreds of proteins and sugar-dependent growth in Arabidopsis. *Plant Cell* **35**, 1318-1333, doi:10.1093/plcell/koad023 (2023).
31 Branon, T. C. *et al.* Efficient proximity labeling in living cells and organisms with TurboID. *Nat Biotechnol* **36**, 880-887, doi:10.1038/nbt.4201 (2018).
32 Xu, S. L., Shrestha, R., Karunadasa, S. S. & Xie, P. Q. Proximity Labeling in Plants. *Annu Rev Plant Biol* **74**, 285-312, doi:10.1146/annurev-arplant-070522-052132 (2023).
33 Rodor, J., Pan, Q., Blencowe, B. J., Eyras, E. & Caceres, J. F. The RNA-binding profile of Acinus, a peripheral component of the exon junction complex, reveals its role in splicing regulation. *RNA* **22**, 1411-1426, doi:10.1261/rna.057158.116 (2016).
34 Day, I. S. *et al.* Interactions of SR45, an SR-like protein, with spliceosomal proteins and an intronic sequence: insights into regulated splicing. *Plant J* **71**, 936-947, doi:10.1111/j.1365-313X.2012.05042.x (2012).
35 Zhang, X. N. & Mount, S. M. Two alternatively spliced isoforms of the Arabidopsis SR45 protein have distinct roles during normal plant development. *Plant Physiol* **150**, 1450-1458, doi:10.1104/pp.109.138180 (2009).
36 Murachelli, A. G., Ebert, J., Basquin, C., Le Hir, H. & Conti, E. The structure of the ASAP core complex reveals the existence of a Pinin-containing PSAP complex. *Nat Struct Mol Biol* **19**, 378-386, doi:10.1038/nsmb.2242 (2012).
37 Mair, A., Xu, S. L., Branon, T. C., Ting, A. Y. & Bergmann, D. C. Proximity labeling of protein complexes and cell-type-specific organellar proteomes in Arabidopsis enabled by TurboID. *Elife* **8**, doi:10.7554/eLife.47864 (2019).
38 Shrestha, R. *et al.* 15N Metabolic Labeling Quantification Workflow in Arabidopsis Using Protein Prospector. *Front. Plant Sci.* **13**, 832562, doi:10.3389/fpls.2022.832562 (2022).
39 Otasek, D., Morris, J. H., Boucas, J., Pico, A. R. & Demchak, B. Cytoscape Automation: empowering workflow-based network analysis. *Genome Biol* **20**, 185, doi:10.1186/s13059-019-1758-4 (2019).
40 Francette, A. M. & Arndt, K. M. Multiple direct and indirect roles of the Paf1 complex in transcription elongation, splicing, and histone modifications. *Cell Rep* **43**, 114730, doi:10.1016/j.celrep.2024.114730 (2024).
41 Huang, Y. *et al.* Epigenetic regulation of female germline development through ERECTA signaling pathway. *New Phytol* **240**, 1015-1033, doi:10.1111/nph.19217 (2023).
42 Xiao, C. *et al.* Arabidopsis DXO1 activates RNMT1 to methylate the mRNA guanosine cap. *Nat Commun* **14**, 202, doi:10.1038/s41467-023-35903-8 (2023).
43 Rodriguez Gallo, M. C. & Uhrig, R. G. Phosphorylation mediated regulation of RNA splicing in plants. *Front Plant Sci* **14**, 1249057, doi:10.3389/fpls.2023.1249057 (2023).
44 Li, Y. *et al.* SKIP regulates environmental fitness and floral transition by forming two distinct complexes in Arabidopsis. *New Phytol* **224**, 321-335, doi:10.1111/nph.15990 (2019).
45 Kanno, T., Lin, W. D., Chang, C. L., Matzke, M. & Matzke, A. J. M. A Genetic Screen Identifies PRP18a, a Putative Second Step Splicing Factor Important for Alternative Splicing and a Normal Phenotype in Arabidopsis thaliana. *G3 (Bethesda)* **8**, 1367-1377, doi:10.1534/g3.118.200022 (2018).
46 Krzyszton, M. *et al.* Defective XRN3-mediated transcription termination in Arabidopsis affects the expression of protein-coding genes. *Plant J* **93**, 1017-1031, doi:10.1111/tpj.13826 (2018).
47 Kanno, T. *et al.* PRP4KA, a Putative Spliceosomal Protein Kinase, Is Important for Alternative Splicing and Development in Arabidopsis thaliana. *Genetics* **210**, 1267-1285, doi:10.1534/genetics.118.301515 (2018).

48 de Francisco Amorim, M. *et al.* The U1 snRNP Subunit LUC7 Modulates Plant Development and Stress Responses via Regulation of Alternative Splicing. *Plant Cell* **30**, 2838-2854, doi:10.1105/tpc.18.00244 (2018).
49 Calderon-Villalobos, L. I. *et al.* The evolutionarily conserved TOUGH protein is required for proper development of Arabidopsis thaliana. *Plant Cell* **17**, 2473-2485, doi:10.1105/tpc.105.031302 (2005).
50 Lu, Q. *et al.* Arabidopsis homolog of the yeast TREX-2 mRNA export complex: components and anchoring nucleoporin. *Plant J* **61**, 259-270, doi:10.1111/j.1365-313X.2009.04048.x (2010).
51 Rossell, D., Stephan-Otto Attolini, C., Kroiss, M. & Stocker, A. Quantifying Alternative Splicing from Paired-End Rna-Sequencing Data. *Ann Appl Stat* **8**, 309-330, doi:10.1214/13-aoas687 (2014).
52 Armeev, G. A., Kniazeva, A. S., Komarova, G. A., Kirpichnikov, M. P. & Shaytan, A. K. Histone dynamics mediate DNA unwrapping and sliding in nucleosomes. *Nat Commun* **12**, 2387, doi:10.1038/s41467-021-22636-9 (2021).
53 Pan, S. *et al.* Arabidopsis DXO1 possesses deNADding and exonuclease activities and its mutation affects defense-related and photosynthetic gene expression. *J Integr Plant Biol* **62**, 967-983, doi:10.1111/jipb.12867 (2020).
54 Hartweck, L. M., Scott, C. L. & Olszewski, N. E. Two O-linked N-acetylglucosamine transferase genes of Arabidopsis thaliana L. Heynh. have overlapping functions necessary for gamete and seed development. *Genetics* **161**, 1279-1291, doi:10.1093/genetics/161.3.1279 (2002).
55 Jiang, Y. *et al.* Post-translational modification of SPATULA by SECRET AGENT and SPINDLY promotes organ symmetry transition at the gynoecium apex. *bioRxiv*, doi:10.1101/2023.04.28.538690 (2023).
56 Xing, L. *et al.* O-GlcNAc transferase SEC activates histone methyltransferase ATX1 to regulate flowering. *EMBO J.* **37**, doi:10.15252/embj.201798115 (2018).
57 Will, C. L. & Luhrmann, R. Spliceosome structure and function. *Cold Spring Harb Perspect Biol* **3**, doi:10.1101/cshperspect.a003707 (2011).
58 Chen, W. & Moore, M. J. The spliceosome: disorder and dynamics defined. *Curr Opin Struct Biol* **24**, 141-149, doi:10.1016/j.sbi.2014.01.009 (2014).
59 Bentley, D. L. Coupling mRNA processing with transcription in time and space. *Nat Rev Genet* **15**, 163-175, doi:10.1038/nrg3662 (2014).
60 Yang, J., Cao, Y. & Ma, L. Co-Transcriptional RNA Processing in Plants: Exploring from the Perspective of Polyadenylation. *Int J Mol Sci* **22**, doi:10.3390/ijms22073300 (2021).
61 Blijlevens, M., Li, J. & van Beusechem, V. W. Biology of the mRNA Splicing Machinery and Its Dysregulation in Cancer Providing Therapeutic Opportunities. *Int J Mol Sci* **22**, doi:10.3390/ijms22105110 (2021).
62 Giudice, J. & Jiang, H. Splicing regulation through biomolecular condensates and membraneless organelles. *Nat Rev Mol Cell Biol* **25**, 683-700, doi:10.1038/s41580-024-00739-7 (2024).
63 Shefer, K., Sperling, J. & Sperling, R. The Supraspliceosome - A Multi-Task Machine for Regulated Pre-mRNA Processing in the Cell Nucleus. *Comput Struct Biotechnol J* **11**, 113-122, doi:10.1016/j.csbj.2014.09.008 (2014).
64 Mergner, J. *et al.* Mass-spectrometry-based draft of the Arabidopsis proteome. *Nature* **579**, 409-414, doi:10.1038/s41586-020-2094-2 (2020).
65 Zentella, R. *et al.* O-GlcNAcylation of master growth repressor DELLA by SECRET AGENT modulates multiple signaling pathways in Arabidopsis. *Genes Dev.* **30**, 164-176, doi:10.1101/gad.270587.115 (2016).

66 Zentella, R. *et al.* The Arabidopsis O-fucosyltransferase SPINDLY activates nuclear growth repressor DELLA. *Nat. Chem. Biol.* **13**, 479-485, doi:10.1038/nchembio.2320 (2017).
67 Aoyama, T. & Chua, N. H. A glucocorticoid-mediated transcriptional induction system in transgenic plants. *Plant J* **11**, 605-612, doi:10.1046/j.1365-313x.1997.11030605.x (1997).
68 Stephens, M. False discovery rates: a new deal. *Biostatistics* **18**, 275-294, doi:10.1093/biostatistics/kxw041 (2017).

Figure legend

Fig. 1: Schematic representation of PL-MS for mapping the ACINUS-mediated alternative splicing spliceosome and functional analysis. a. Schematic of TurboID-based interactome mapping. Three bait proteins- ACINUS, PININ, SR45- are fused to the TurboID (TD) proximity labeling enzyme and a VENUS tag, while the control is TD-YFP, expressed under native promoter. Proteins within the labeling radius (blue cloud) are labeled with biotin (red dot), which is enriched by streptavidin beads followed by mass spectrometric analysis. After comparison with the control, the enriched protein list from each bait is overlapped and filtered to generate a highly reliable interactome list. **b**. Construct information of the bait and corresponding control. All constructs contain V5 and VENUS or YFP tags. Controls contain a nuclear localization signal (NLS). **c.** Confocal microscopy shows that the ACINUS-TD, ACINUSΔRSB-TD, PININ-TD, and SR45-TD fusion proteins localize to the nucleus. **d**. ACINUS-TD, PNN-TD and SR45-TD fusion proteins rescued the corresponding mutants to wild-type levels.

Fig. 2: Comprehensive high-confidence PL-MS mapping of the ACINUS-proxiome. a. Schematic of protein-level enrichment for mapping the ACINUS proxiome. Baits and controls were treated with biotin (n=3 biological replicates) followed by protein-level enrichment. **b-d**. Volcano plots of ACINUS-TD, PNN-TD, and SR45-TD. Proteins enriched by either the bait (right) or the controls (left) are highlighted as red dots. The bait proteins, known interactors, and novel interactors are marked and highlighted in black, red, or blue, respectively. Some nuclear proteins biotinylated by Turbo-YFP controls are marked. **e**. Schematic of peptide-level enrichment for mapping the ACINUS-proxiome. After SILIA labeling, protein extraction, and tryptic digestion, the biotinylated peptides were enriched with streptavidin beads. **f.** Quantification of ACINUS-TD data using peptide-level enrichment. Bait-enriched proteins are highlighted as red dots, biotinylated nuclear proteins and endogenous biotinylated proteins are highlighted as blue dots. Unmodified proteins that show equal mixing are shown as black dots. The bait proteins, known interactors, and novel interactors are marked and highlighted in black, red, or blue. **g**. A confidence list is generated after extensive filtering and comparison of TurboID vs IP-MS. **h**. Over 75% of the ACINUS-TD interactors show reduced or lost interactions in ACINUSΔRSB-TD. **i.** Go analysis of the ACINUS proxiome shows significant enrichment in mRNA processing.

Fig 3. Cytoscape of the ACINUS-proxiome showing co-transcriptional, co-occurring activity of mRNA processing and high redundancy. a. The ACINUS-proxiome network is visualized in Cytoscape, integrating TurboID, STRING and GRID data. Nodes represent proteins and edges indicate interactions between them, as shown by gray lines. Proteins from STRING and GRID are circled based on connectivity: nodes with 10-109 edges are bordered in magenta, those with 3-9 degrees are bordered in blue, those with 1-2 edges are bordered in green, and those with no edges are bordered in yellow. Proteins with known or predicted functions are grouped and color-coded as follows: NTC complex filled in gray; A, B/B^{act}, and C complex proteins are filled in green, yellow, and pink, respectively; core and accessory spliceosome components (U1, U2, U4/U5/U6) are filled in darker pink. Proteins involved in transcription and chromatin modeling are filled in light pink, while proteins involved in m6A methylation, 5' capping, 3' polyadenylation and mRNA export are filled in pink, dark green, light green, and light yellow, respectively.

b. Interpro analysis reveals high redundancy within the AICINUS proxiome. The numbers within the boxes indicate the number of proteins detected with specific domains, while the domain names are labeled at the top.

Fig. 4: Common and distinct alternative splicing events regulated by components in the ACINUS network. a-g. Venn diagram showing the comparison of shared and distinct intron retention events between the *acinus pinin* mutant and several other mutants, along with the corresponding p- value. A representative intron retention event is shown for each comparison, with arrows indicating the retained introns. **h.** Directionality of regulated intron retention events, comparing *acinus pinin* mutants with other selected mutants. **i.** *tgh* and *dxo1* mutants show phenotypes similar to the *acinus pinin* double mutants, including twisted leaves, reduced size, and a pale green color.

Fig 5: SPY and SEC regulate transcription and alternative splicing in an ACINUS-dependent and -independent manner. **a**. Venn diagram showing the overlap of the ACINUS proxiome with the O-GlcNAcylation library and the O-fucosylation library. **b**. Selected proteins in the ACINUS proxiome that are O-GlcNAcylated (blue box), O-fucosylated (red triangle), or by both. **c**. Inducible *shSEC RNAi* in *spy-4* showed reduced root growth after Dex treatment. **d**. Significant overlap of transcriptome changes between *acinus pinin* and *shSEC RNAi spy-4* (+Dex) compared to WT. **e**. Heatmap of 1155 common transcripts across WT, *spy-4*, *shSEC RNAi spy-4* under mock or Dex treatment. **f-g.** Significant overlap of intron retention changes between *acinus pinin* and *shSEC RNAi spy-4* (+Dex) compared to WT (**f**), with an example of increased intron retention in the 9th intron of AT1G48360 (**g**). **h**. Regulated events occur mainly in the same direction by ACINUS/PININ and SPY/SEC. **i**. Comparison of intron retention between *skip* and *spy sec* double mutant reveals some SKIP-dependent manner.

Fig. 6 Model of interdependent mRNA processing and the role of SEC/SPY in regulating alternative splicing and transcription through ACINUS dependent and -independent pathway. a. Alternative splicing involves large complexes and our data suggests that it is intricately linked to other mRNA processing events, including transcription, chromatin modeling, 5' capping, m6A methylation, 3' cleavage and polyadenylation, and mRNA transport. **b.** RNA-seq data suggest that SEC and SPY modulate transcription and alternative splicing through both ACINUS-dependent and ACINUS-independent mechanisms.

Extended Data Fig. 1| ACINUS-TD, PNN-TD, and SR45-TD fusion proteins localize to the nucleus and complement the leaf shape, rosette size, and flowering phenotypes in corresponding mutants. **a**. Spinning disk images of ACINUS-TD, PNN-TD and SR45-TD. Scale =10 µm. **b**. Wild type (WT), mutants, and two independent complementation lines of each bait were grown in soil for approximately 4 weeks, showing the complementation of the leaf shape and rosette size phenotypes. Scale = 1cm. **c**. The same plants were grown in the greenhouse for about 6 weeks, showing the complementation of the flowering time phenotype by the TurboID fusion proteins. Scale bar=5 cm.

Extended Data Fig. 2| Representative spectra for identification and quantification of ^{14}N- and ^{15}N-labeled biotinylated peptides from SRPK5 protein. a-b, MS2 spectra of *m/z* 586.3122 and 591.9615, 3+ precursors, identified a ^{14}N-labeled (**a**) or ^{15}N-labeled (**b**) biotinylated peptide from SRPK5 spanning from amino acid 208 - 221 with a modification on K209, detected in ACINUS-TD enriched samples. The signature ion corresponding to derivative ion at *m/z* 310.16 (^{14}N) or 311.16 (^{15}N) due to the ammonia loss of the immonium ion of biotinylated lysine (ImKBio) is labeled with the measured mass. **c.** Quantitative spectra showing the MS1 peak matches. Three peaks corresponding to M, M+1, M+2 peaks are highlighted in red for upper ^{14}N-labeled peaks and the lower ^{15}N-labeled peaks from forward 1(Fw1) and reverse 1 (Rv1) experiments. Monoisotopic peaks are indicated by arrows, with ^{14}N shown in blue and ^{15}N in red.

Extended Data Fig. 3 | High-confidence quantification of TurboID and functional analysis of ACINUSΔRSB complementation. a. Venn diagram of overlap of enriched proteins based on protein-level enrichment only. **b.** Comparative analysis between ACINUS-TD vs ACINUSΔRSB-TD shows a significant reduction or dramatic loss of interactions in ACINUSΔRSB-TD. Only pre-filtered ACINUS-TD interactors from the protein-level enrichment were plotted. Proteins with more than 2-fold difference and a p-value=0.05 are highlighted in red. ACINUS, SR45 and SAP18 are labeled. **c.** Quantification of selected proteins across different experiments, including a non-specific control protein HOP1 and several ACINUS interactors, shows reduced or lost interactions in ACINUSΔRSB. **d.** Expression of ACINUSΔRSB expressed in the *acinus pnn* mutant still displays narrow and twisted leaves, but partially rescues the phenotype, leading to significantly larger leaves compared to the *acinus pnn* mutant alone. **e**. Quantification of leaf lengths of ACINUSΔRSB- TD/ap independent lines and the ap mutant. Leaf lengths were measured from plants grown for 13 days on soil under 16 h light/8 h dark conditions. Measurements were obtained from more than 15 plants per genotype. Statistical significance was determined with $P < 0.01$.

Extended Data Fig. 4 | Enhanced intron retention analysis pipeline and comparison of selected mutants.

a. Enhanced intron retention analysis pipeline. The left panel shows intron coverage ratio (ICratio) used by Bi et al., 2021, while the right panel shows intron depth ratio (IDratio). The main filtering steps are also listed. **b.** UpSet plot shows the overlapping and distinct intron retention across all selected mutants.

Extended data Fig. 5 | The inducible *shSEC RNAi spy-4* line shows seedling lethality. a. Schematic of Dex-inducible *shSEC RNAi* construct compared to *a2SEC RNAi*. Genomic and cDNA of SEC segments are cloned in a head-to-head orientation to pTA7002 to generate the short hairpin RNAi. **b.** Seedling lethality was observed when double mutants were grown directly on Dex-supplemented plates. **c**. Progressive phenotype of *shSEC RNAi spy-4* phenotype after Dex treatment, showing reduced root growth by day 3, leaf discoloration by day 5 and complete growth arrest by day 7. **d**. Quantification of root elongation after transfer on mock and Dex treatment. Root lengths were measured in over 15 seedlings, and statistical analysis was performed using a two-tailed t-test ($p < 0.001$).

Extended data Fig. 6 | PCA analysis of RNA-seq results and comparison of altered transcript. a. PCA analysis of transcriptomics data from WT, *acinus pinin*, *spy-4*, *shSEC RNAi spy-4* (with and without Dex treatment) shows distinct clustering of each group, as well as clustering between *spy-4* and *shSEC RNAi spy-4* groups. **b**. Heatmap depicting 8199 transcripts that are altered in *acinus pinin*, *shSEC RNAi spy-4* (with Dex), or both.

Supplemental Table

Supplemental Table 1: TurboID-related results. The table includes Table content TurboID summary, Evolution conserveness, ACINUS-TD_Protein-level result, PNN-TD_Protein-level result, SR45-TD_Protein-level result, Comparison of ACINUS-TD vs ACINUSΔRSB-TD, ACINUS-TD_Peptide Level, Interpro Results, and Interpro results counts.

Supplemental Table 2: Primers used in this study.

Supplemental Table 3: RNA-seq analysis result.

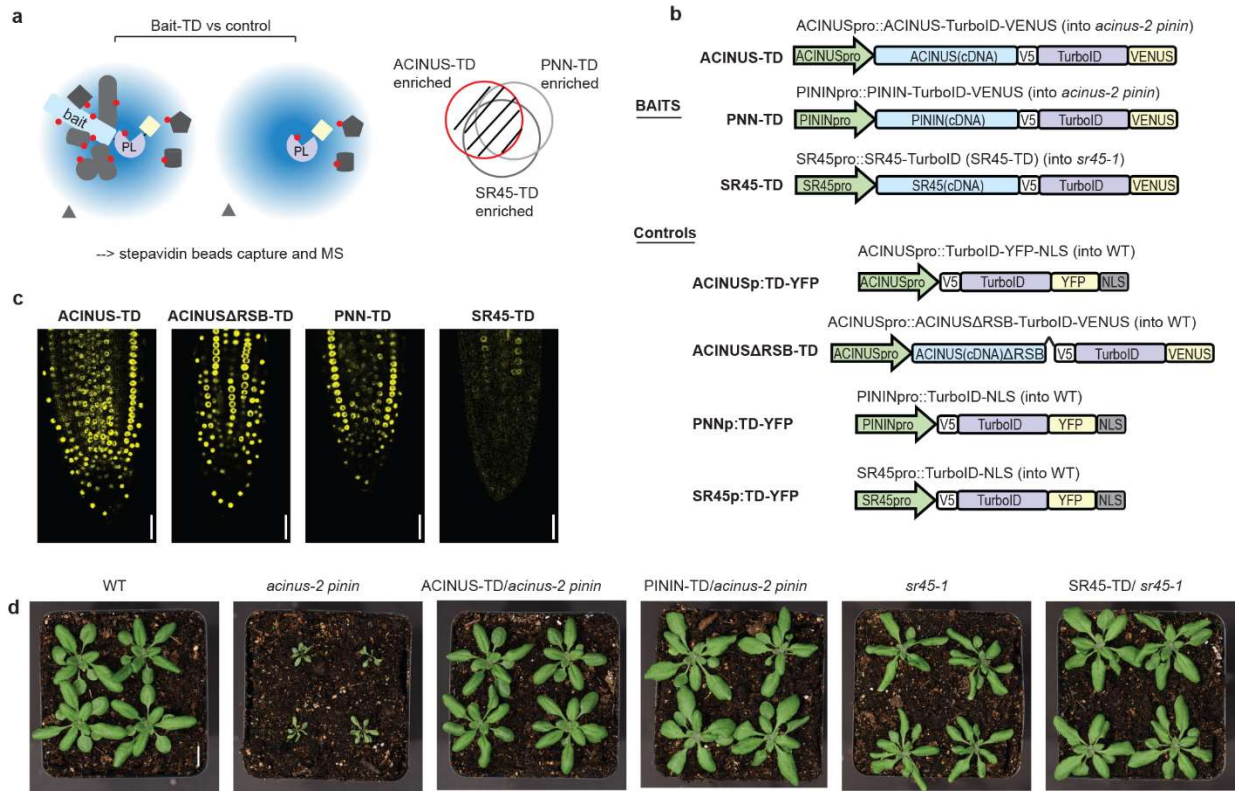

Fig. 1: Schematic representation of PL-MS for mapping the ACINUS-mediated alternative splicing spliceosome and functional analysis. a. Schematic of TurboID-based interactome mapping. Three bait proteins- ACINUS, PININ, SR45- are fused to the TurboID (TD) proximity labeling enzyme and a VENUS tag, while the control is TD-YFP, expressed under native promoter. Proteins within the labeling radius (blue cloud) are labeled with biotin (red dot), which is enriched by streptavidin beads followed by mass spectrometric analysis. After comparison with the control, the enriched protein list from each bait is overlapped and filtered to generate a highly reliable interactome list. **b**. Construct information of the bait and corresponding control. All constructs contain V5 and VENUS or YFP tags. Controls contain a nuclear localization signal (NLS). **c.** Confocal microscopy shows that the ACINUS-TD, ACINUSΔRSB-TD, PININ-TD, and SR45-TD fusion proteins localize to the nucleus. **d**. ACINUS-TD, PNN-TD and SR45-TD fusion proteins rescued the corresponding mutants to wild-type levels.

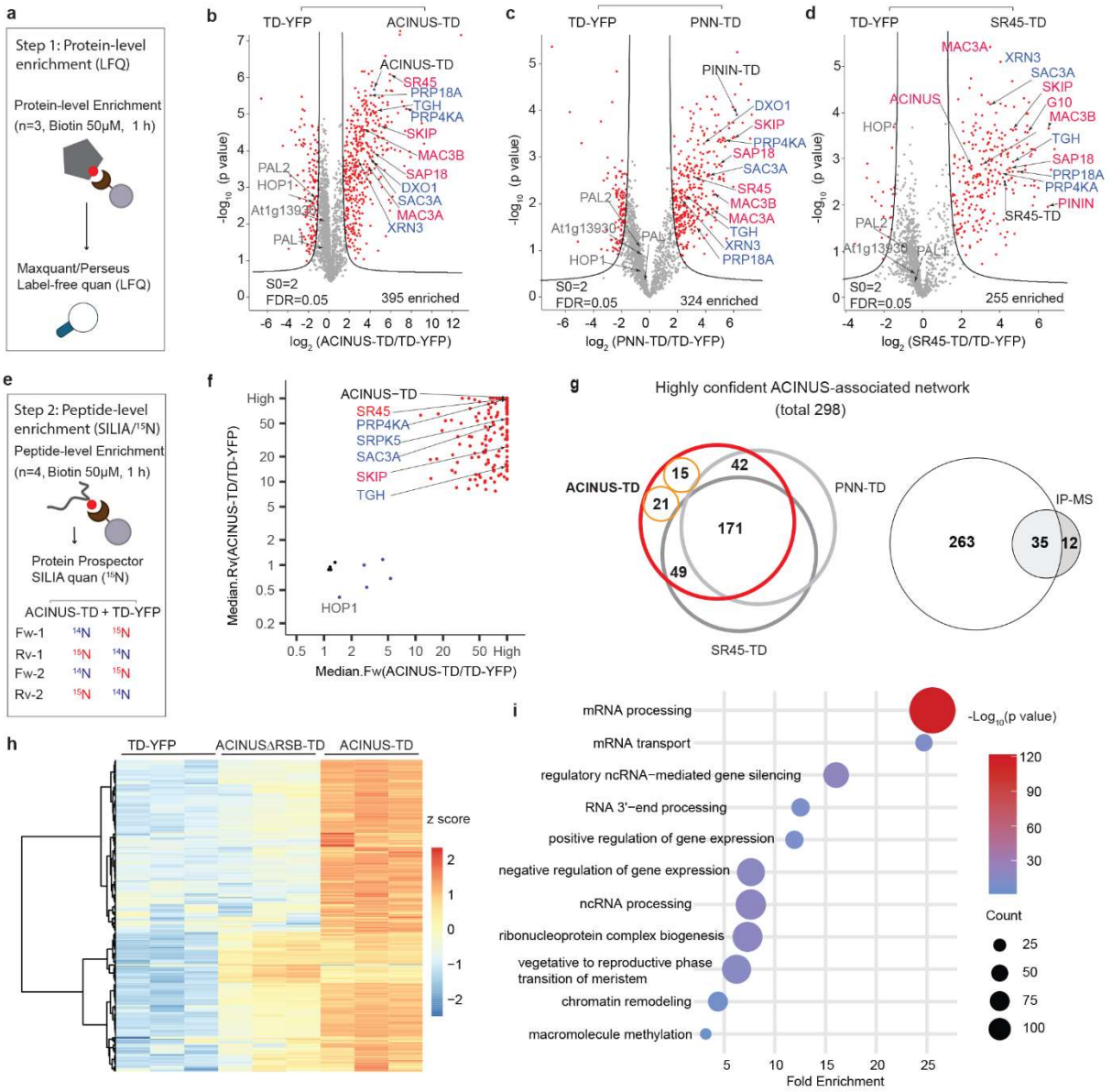

Fig. 2: Comprehensive high-confidence PL-MS mapping of the ACINUS-proxiome. a. Schematic of protein-level enrichment for mapping the ACINUS proxiome. Baits and controls were treated with biotin (n=3 biological replicates) followed by protein-level enrichment. **b-d**. Volcano plots of ACINUS-TD, PNN-TD, and SR45-TD. Proteins enriched by either the bait (right) or the controls (left) are highlighted as red dots. The bait proteins, known interactors, and novel interactors are marked and highlighted in black, red, or blue, respectively. Some nuclear proteins biotinylated by Turbo-YFP controls are marked. **e**. Schematic of peptide-level enrichment for mapping the ACINUS-proxiome. After SILIA labeling, protein extraction, and tryptic digestion, the biotinylated peptides were enriched with streptavidin beads. **f.** Quantification of ACINUS-TD data using peptide-level enrichment. Bait-enriched proteins are highlighted as red dots, biotinylated nuclear proteins and endogenous biotinylated proteins are highlighted as blue dots. Unmodified proteins that show equal mixing are shown as black dots. The bait proteins, known interactors, and novel interactors are marked and highlighted in black, red, or blue. **g**. A confidence list is

generated after extensive filtering and comparison of TurboID vs IP-MS. **h**. Over 75% of the ACINUS-TD interactors show reduced or lost interactions in ACINUSΔRSB-TD. **i.** Go analysis of the ACINUS proxiome shows significant enrichment in mRNA processing.

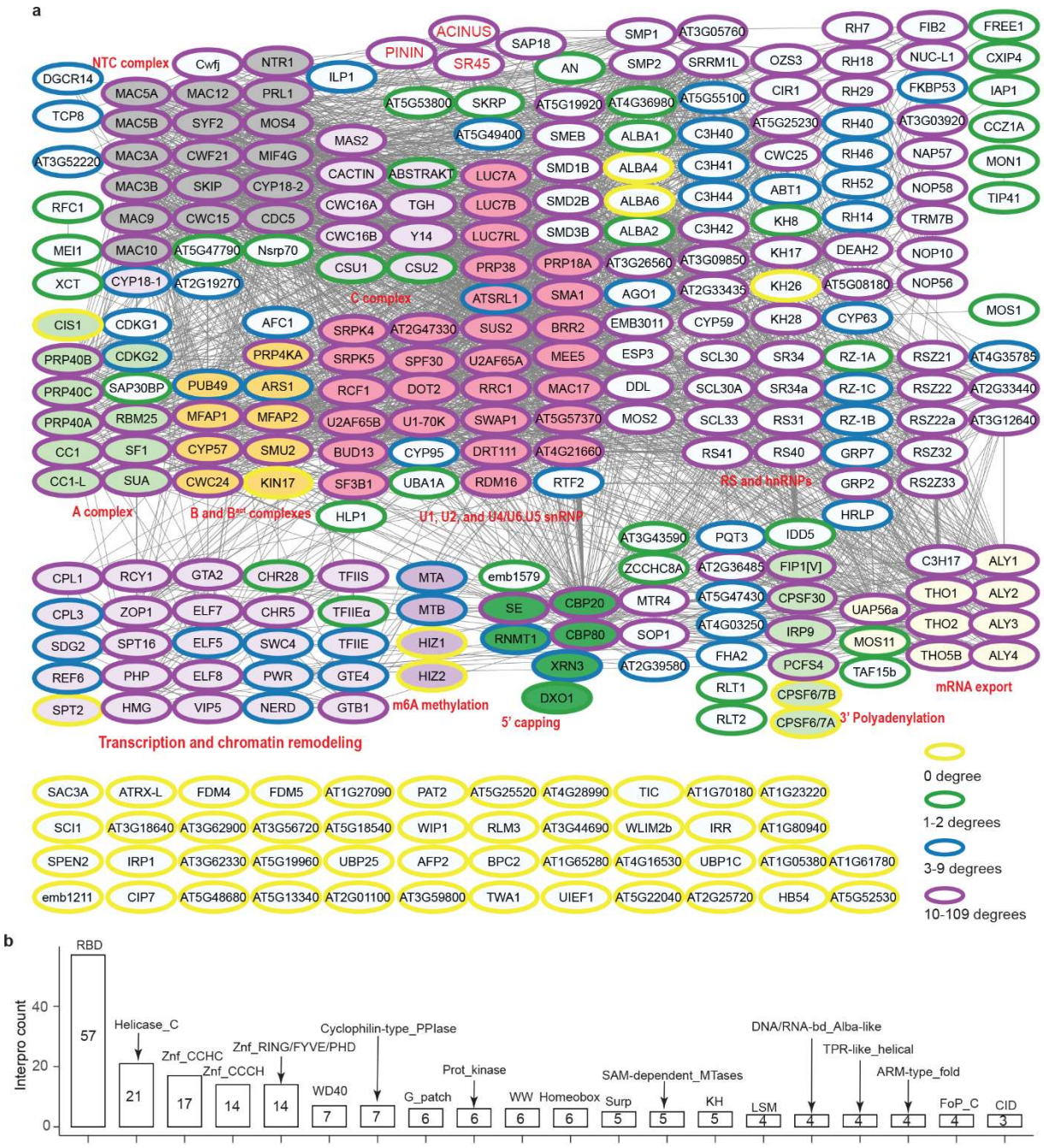

Fig 3. Cytoscape of the ACINUS-proxiome showing co-transcriptional, co-occurring activity of mRNA processing and high redundancy. a. The ACINUS-proxiome network is visualized in Cytoscape, integrating TurboID, STRING and GRID data. Nodes represent proteins and edges indicate interactions between them, as shown by gray lines. Proteins from STRING and GRID are circled based on connectivity: nodes with 10-109 edges are bordered in magenta, those with 3-9 degrees are bordered in blue, those with 1-2 edges are bordered in green, and those with no edges are bordered in yellow. Proteins with known or predicted functions are grouped and color-coded as follows: NTC complex filled in gray; A, B/B^{act}, and C complex proteins are filled in green, yellow, and pink, respectively; core and accessory spliceosome components

(U1, U2, U4/U5/U6) are filled in darker pink. Proteins involved in transcription and chromatin modeling are filled in light pink, while proteins involved in m6A methylation, 5' capping, 3' polyadenylation and mRNA export are filled in pink, dark green, light green, and light yellow, respectively. **b**. Interpro analysis reveals high redundancy within the AICINUS proxiome. The numbers within the boxes indicate the number of proteins detected with specific domains, while the domain names are labeled at the top.

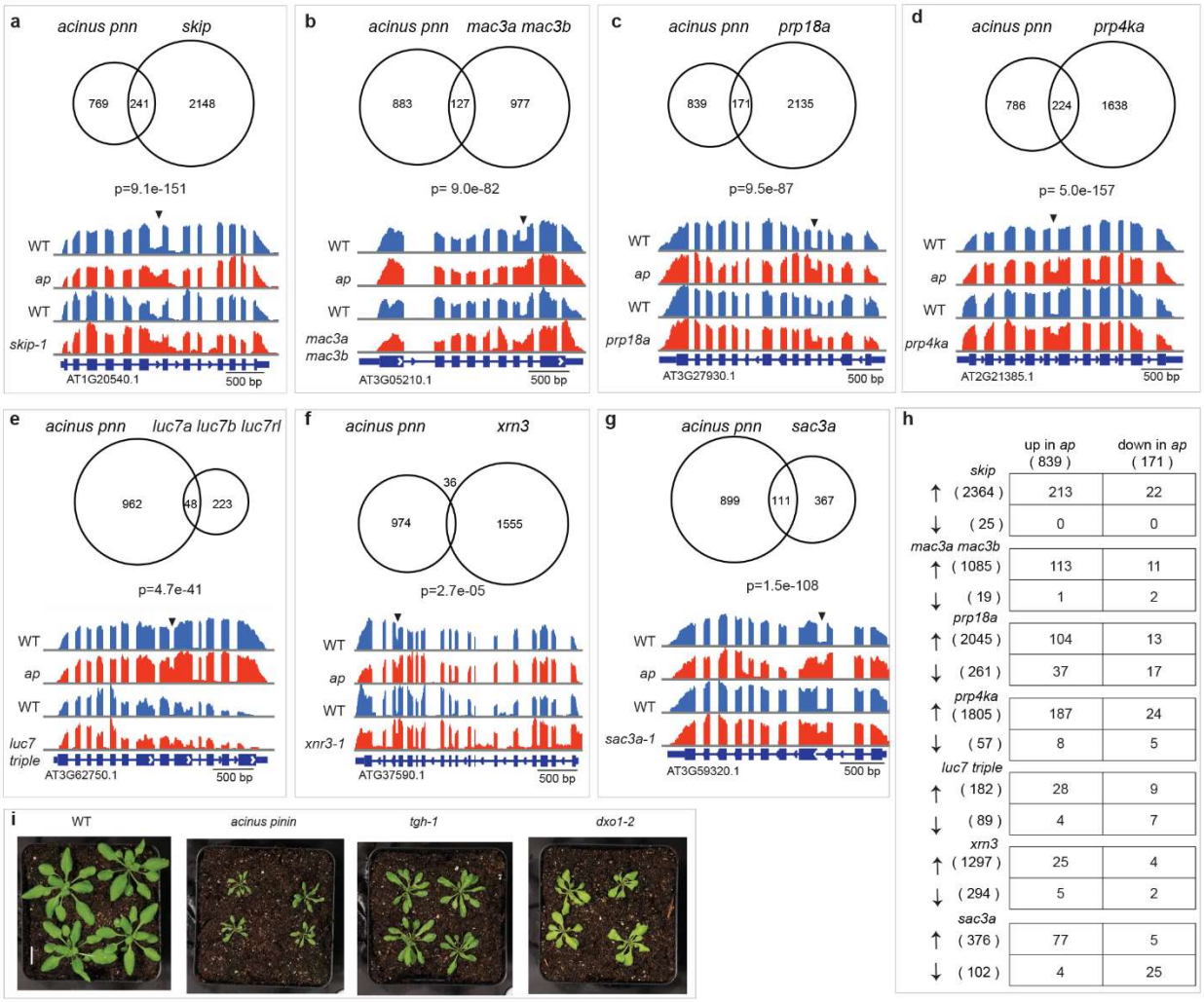

		up in *ap* (839)	down in *ap* (171)
skip			
↑	(2364)	213	22
↓	(25)	0	0
mac3a mac3b			
↑	(1085)	113	11
↓	(19)	1	2
prp18a			
↑	(2045)	104	13
↓	(261)	37	17
prp4ka			
↑	(1805)	187	24
↓	(57)	8	5
luc7 triple			
↑	(182)	28	9
↓	(89)	4	7
xrn3			
↑	(1297)	25	4
↓	(294)	5	2
sac3a			
↑	(376)	77	5
↓	(102)	4	25

Fig. 4: Common and distinct alternative splicing events regulated by components in the ACINUS network. a-g. Venn diagram showing the comparison of shared and distinct intron retention events between the *acinus pinin* mutant and several other mutants, along with the corresponding p- value. A representative intron retention event is shown for each comparison, with arrows indicating the retained introns. **h.** Directionality of regulated intron retention events, comparing *acinus pinin* mutants with other selected mutants. **i.** *tgh* and *dxo1* mutants show phenotypes similar to the *acinus pinin* double mutants, including twisted leaves, reduced size, and a pale green color.

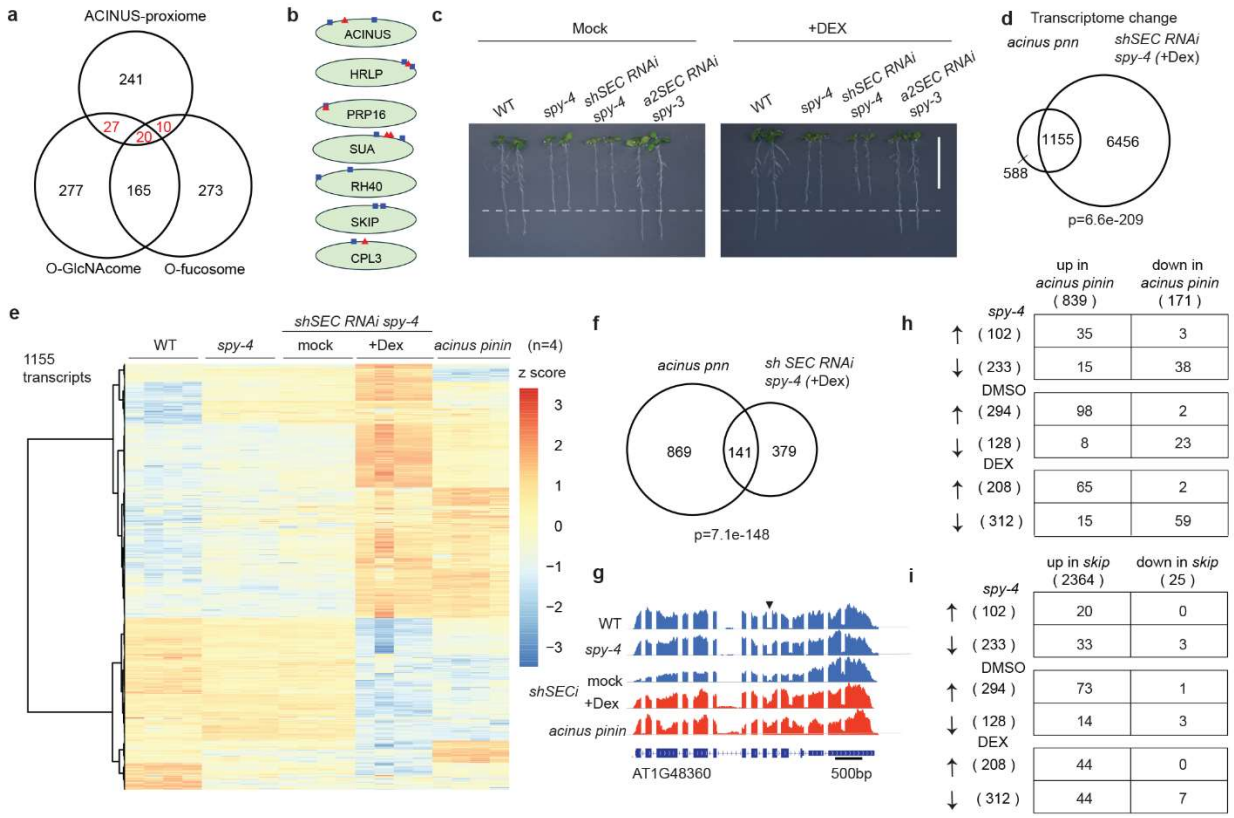

Fig 5: SPY and SEC regulate transcription and alternative splicing in an ACINUS-dependent and -independent manner. **a**. Venn diagram showing the overlap of the ACINUS proxiome with the O-GlcNAcylation library and the O-fucosylation library. **b**. Selected proteins in the ACINUS proxiome that are O-GlcNAcylated (blue box), O-fucosylated (red triangle), or by both. **c**. Inducible *shSEC RNAi* in *spy-4* showed reduced root growth after Dex treatment. **d**. Significant overlap of transcriptome changes between *acinus pinin* and *shSEC RNAi spy-4* (+Dex) compared to WT. **e**. Heatmap of 1155 common transcripts across WT, *spy-4*, *shSEC RNAi spy-4* under mock or Dex treatment. **f-g.** Significant overlap of intron retention changes between *acinus pinin* and *shSEC RNAi spy-4* (+Dex) compared to WT (**f**), with an example of increased intron retention in the 9th intron of AT1G48360 (**g**). **h**. Regulated events occur mainly in the same direction by ACINUS/PININ and SPY/SEC. **i**. Comparison of intron retention between *skip* and *spy sec* double mutant reveals some SKIP-dependent manner.

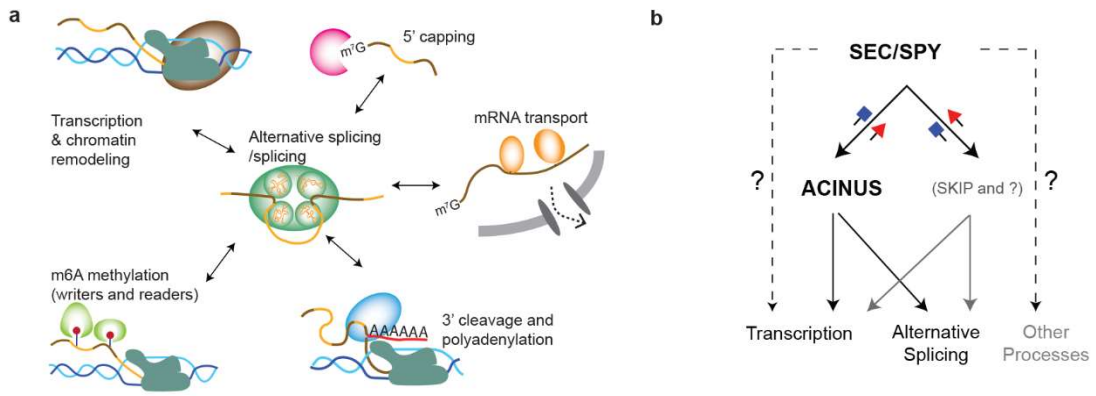

Fig. 6 Model of interdependent mRNA processing and the role of SEC/SPY in regulating alternative splicing and transcription through ACINUS dependent and -independent pathway. a. Alternative splicing involves large complexes and our data suggests that it is intricately linked to other mRNA processing events, including transcription, chromatin modeling, 5' capping, m6A methylation, 3' cleavage and polyadenylation, and mRNA transport. **b.** RNA-seq data suggest that SEC and SPY modulate transcription and alternative splicing through both ACINUS-dependent and ACINUS-independent mechanisms.

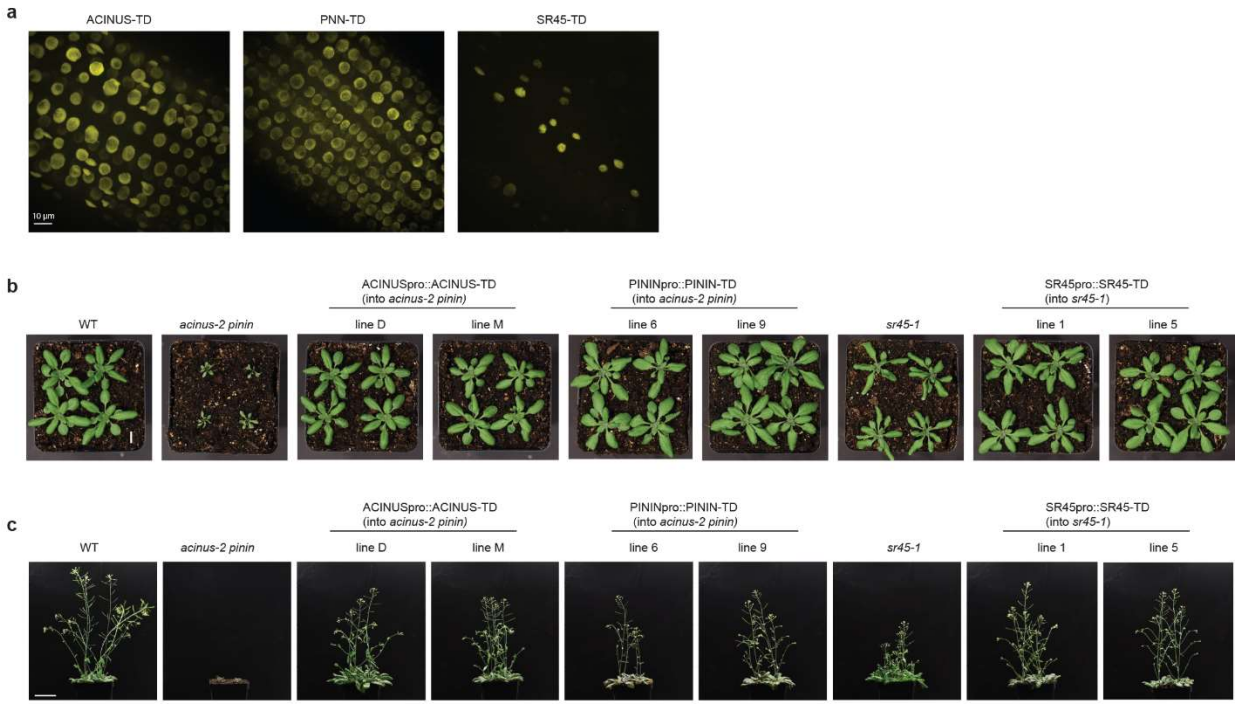

Extended Data Fig. 1| ACINUS-TD, PNN-TD, and SR45-TD fusion proteins localize to the nucleus and complement the leaf shape, rosette size, and flowering phenotypes in corresponding mutants. **a**. Spinning disk images of ACINUS-TD, PNN-TD and SR45-TD. Scale =10 µm. **b**. Wild type (WT), mutants, and two independent complementation lines of each bait were grown in soil for approximately 4 weeks, showing the complementation of the leaf shape and rosette size phenotypes. Scale = 1cm. **c**. The same plants were grown in the greenhouse for about 6 weeks, showing the complementation of the flowering time phenotype by the TurboID fusion proteins. Scale bar=5 cm.

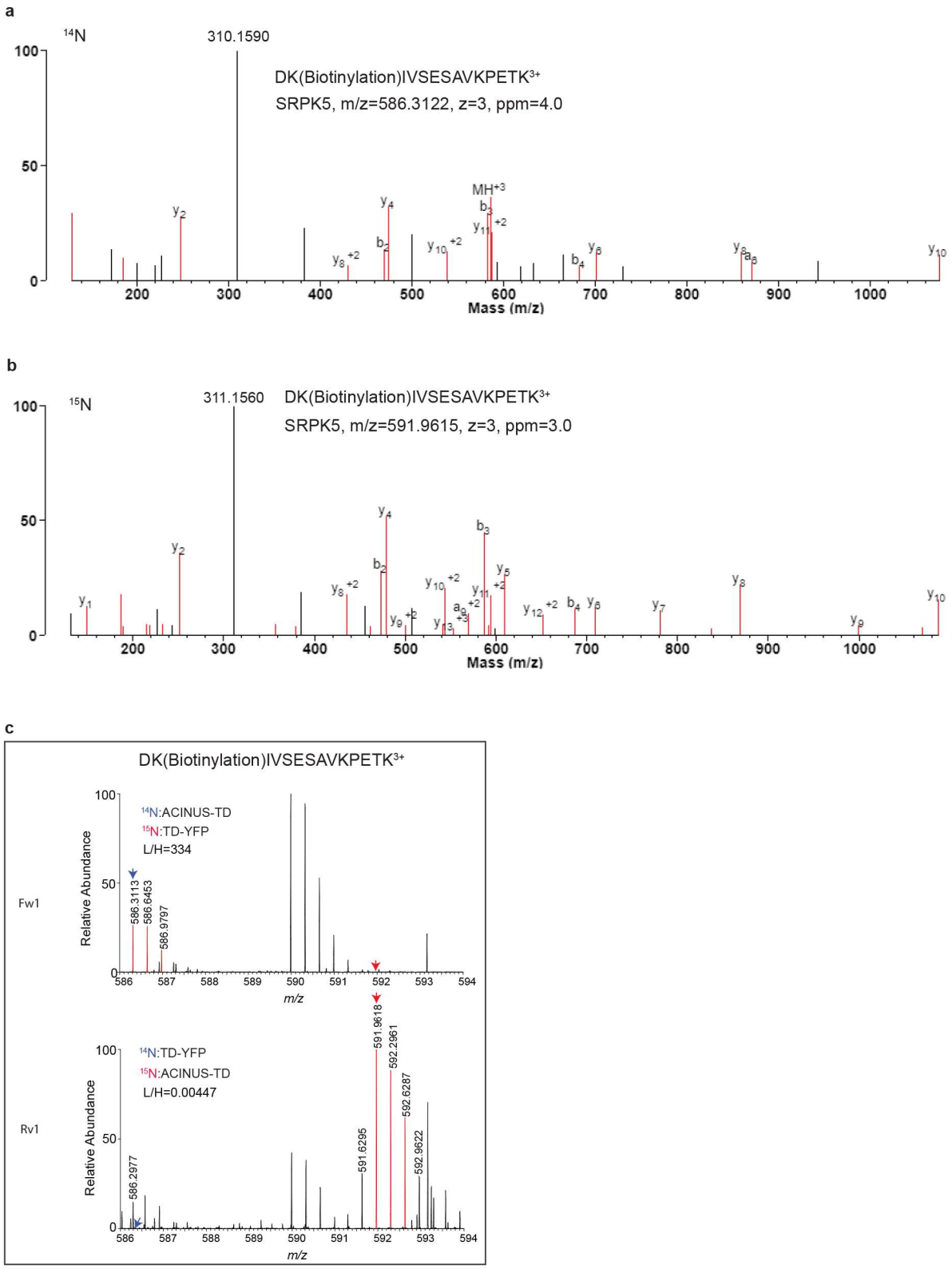

Extended Data Fig. 2| Representative spectra for identification and quantification of ^{14}N- and ^{15}N- labeled biotinylated peptides from SRPK5 protein. a-b, MS2 spectra of *m/z* 586.3122

and 591.9615, 3+ precursors, identified a ^{14}N-labeled (**a**) or ^{15}N-labeled (**b**) biotinylated peptide from SRPK5 spanning from amino acid 208 - 221 with a modification on K209, detected in ACINUS-TD enriched samples. The signature ion corresponding to derivative ion at *m/z* 310.16 (^{14}N) or 311.16 (^{15}N) due to the ammonia loss of the immonium ion of biotinylated lysine (ImKBio) is labeled with the measured mass. **c.** Quantitative spectra showing the MS1 peak matches. Three peaks corresponding to M, M+1, M+2 peaks are highlighted in red for upper ^{14}N-labeled peaks and the lower ^{15}N-labeled peaks from forward 1(Fw1) and reverse 1 (Rv1) experiments. Monoisotopic peaks are indicated by arrows, with ^{14}N shown in blue and ^{15}N in red.

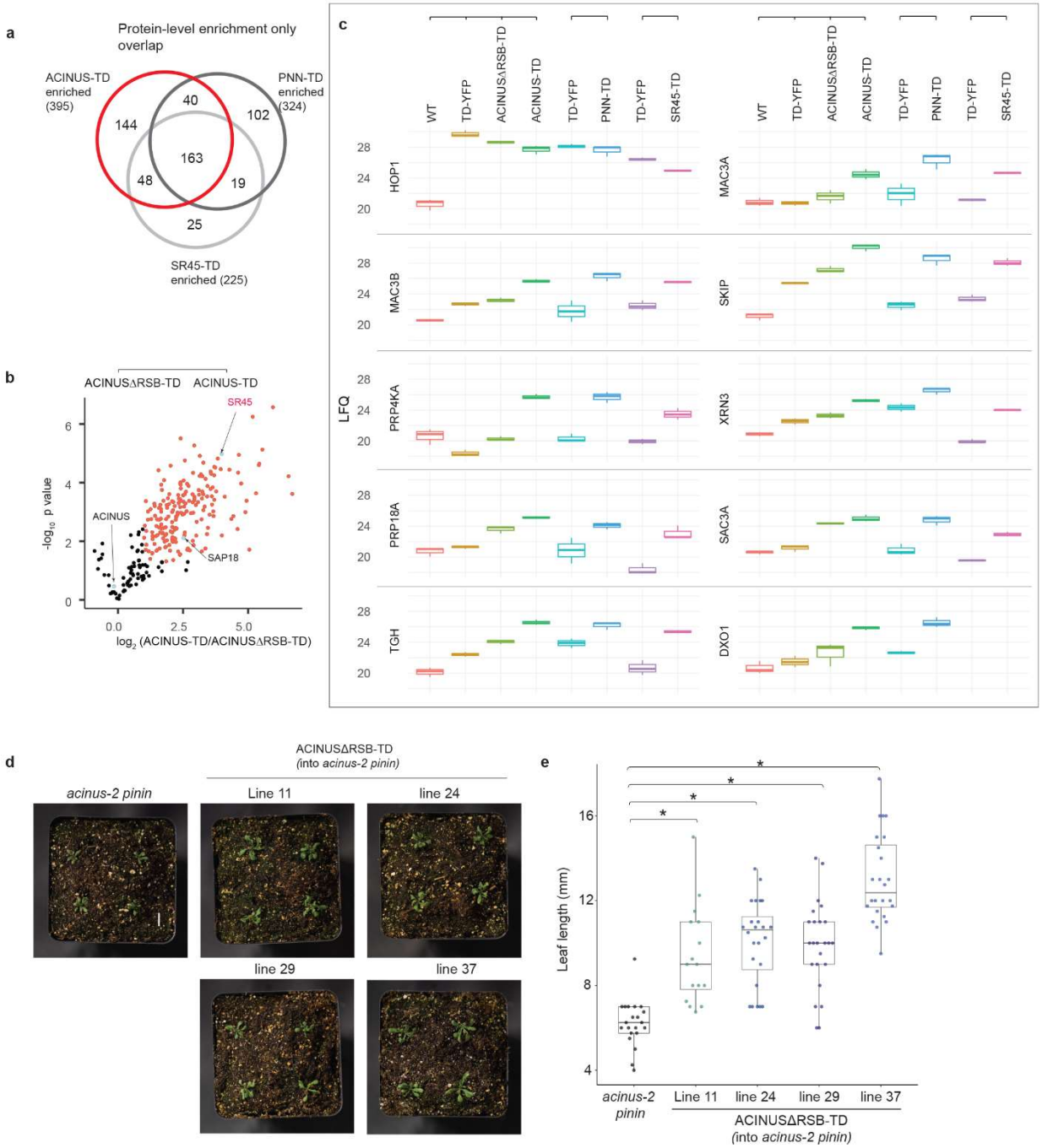

Extended Data Fig. 3 | High-confidence quantification of TurboID and functional analysis of ACINUSΔRSB complementation. a. Venn diagram of overlap of enriched proteins based on protein-level enrichment only. **b.** Comparative analysis between ACINUS-TD vs ACINUSΔRSB-TD shows a significant reduction or dramatic loss of interactions in ACINUSΔRSB-TD. Only pre-filtered ACINUS-TD interactors from the protein-level enrichment were plotted. Proteins with more than 2-fold difference and a p-value=0.05 are highlighted in red. ACINUS, SR45 and SAP18 are labeled. **c.** Quantification of selected proteins across different experiments, including a non-specific control protein HOP1 and several ACINUS interactors, shows reduced or lost

interactions in ACINUSΔRSB. **d.** Expression of ACINUSΔRSB expressed in the *acinus pnn* mutant still displays narrow and twisted leaves, but partially rescues the phenotype, leading to significantly larger leaves compared to the *acinus pnn* mutant alone. **e**. Quantification of leaf lengths of ACINUSΔRSB- TD/ap independent lines and the ap mutant. Leaf lengths were measured from plants grown for 13 days on soil under 16 h light/8 h dark conditions. Measurements were obtained from more than 15 plants per genotype. Statistical significance was determined with $P < 0.01$.

a

Intron retention identification pipeline

List of introns given by sample-sensitive intron-retention (IR) comparison (RACKj).

Bi et al., 2021 ⟷ Shrestha et al., this study

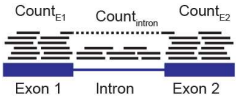

Intron Coverage ratio (ICratio) = $\frac{Count_{intron}}{Count_{E1} + Count_{E2}}$

↓

ICratio Fold change = $\frac{Mean(ICratio_{mut})}{Mean(ICratio_{WT})}$

↓

two-tailed t-test: ICratio $_{mut}$ vs. ICratio $_{WT}$

↓

Filter steps

i) $|ICratio\ Fold\ change| >= 2$

ii) P-Value < = 0.05

iii) Average Intron RPKM in Mutant > 1

iv) $\frac{Intron\ RPKM}{Gene\ RPKM} > 0.05$

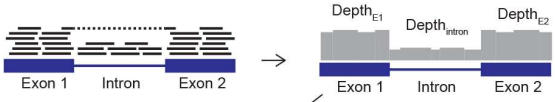

Intron Depth ratio (IDratio) = $\frac{Depth_{intron}}{Mean(Depth_{E1} + Depth_{E2})}$

If Intron is the first intron; IDratio = $\frac{Depth_{intron}}{Depth_{E2}}$

or

If Intron is the last intron; IDratio = $\frac{Depth_{intron}}{Depth_{E1}}$

↓

log_2 transformed

↓

two-tailed t-test: log_2(IDratio $_{mut}$) vs. log_2 (IDratio $_{WT}$)

↓

Imputation of log_2 (IDratio $_{WT}$) if they are infinity

↓

IDratio Fold change = Mean (log_2(IDratio $_{mut}$)) - Mean(log_2(IDR $_{WT}$))

↓

Filter steps

i) P-Value < = 0.05

ii) Intron Depth Ratio Fold change >= 0.58

iii) Average Gene RPKM in Mutant > 1

iv) average depth of 5

v) Filter genes with only one intron

vi) Mean(IDratio $_{mut}$) >= 0.15

b

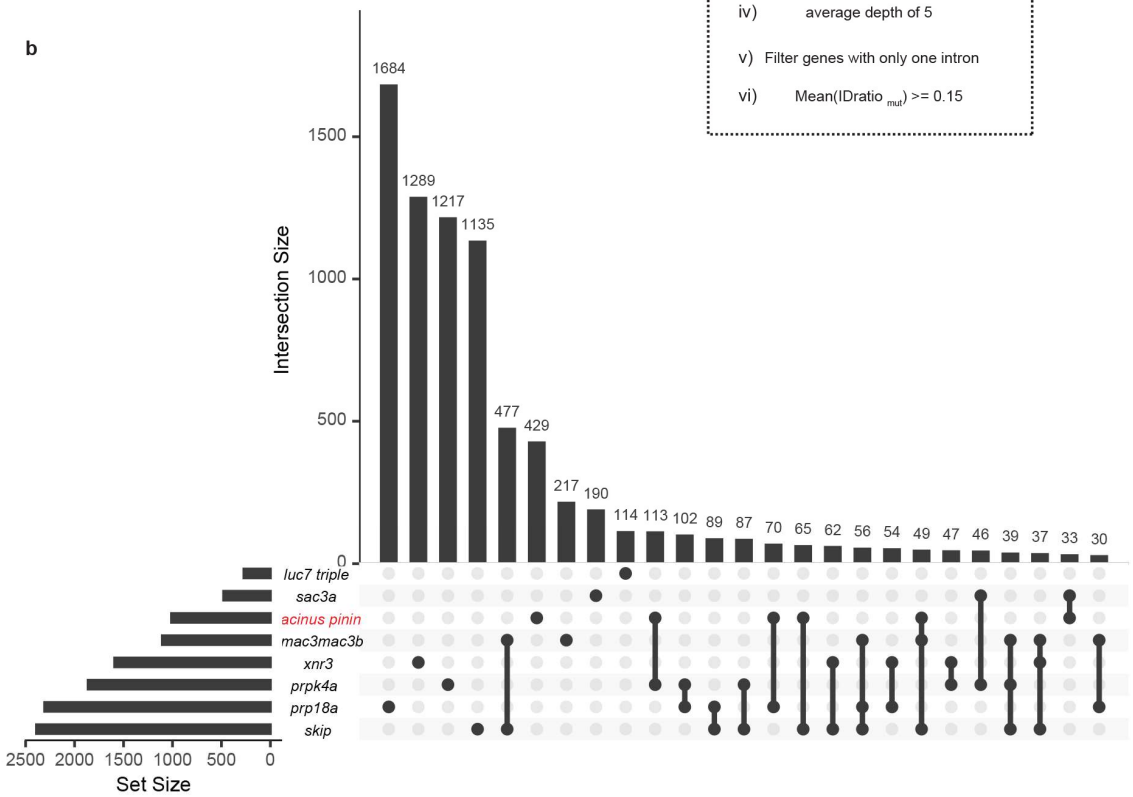

Extended Data Fig. 4 | Enhanced intron retention analysis pipeline and comparison of selected mutants. a. Enhanced intron retention analysis pipeline. The left panel shows intron coverage ratio (ICratio) used by Bi et al., 2021, while the right panel shows intron depth ratio (IDratio). The main filtering steps are also listed. **b.** UpSet plot shows the overlapping and distinct intron retention across all selected mutants.

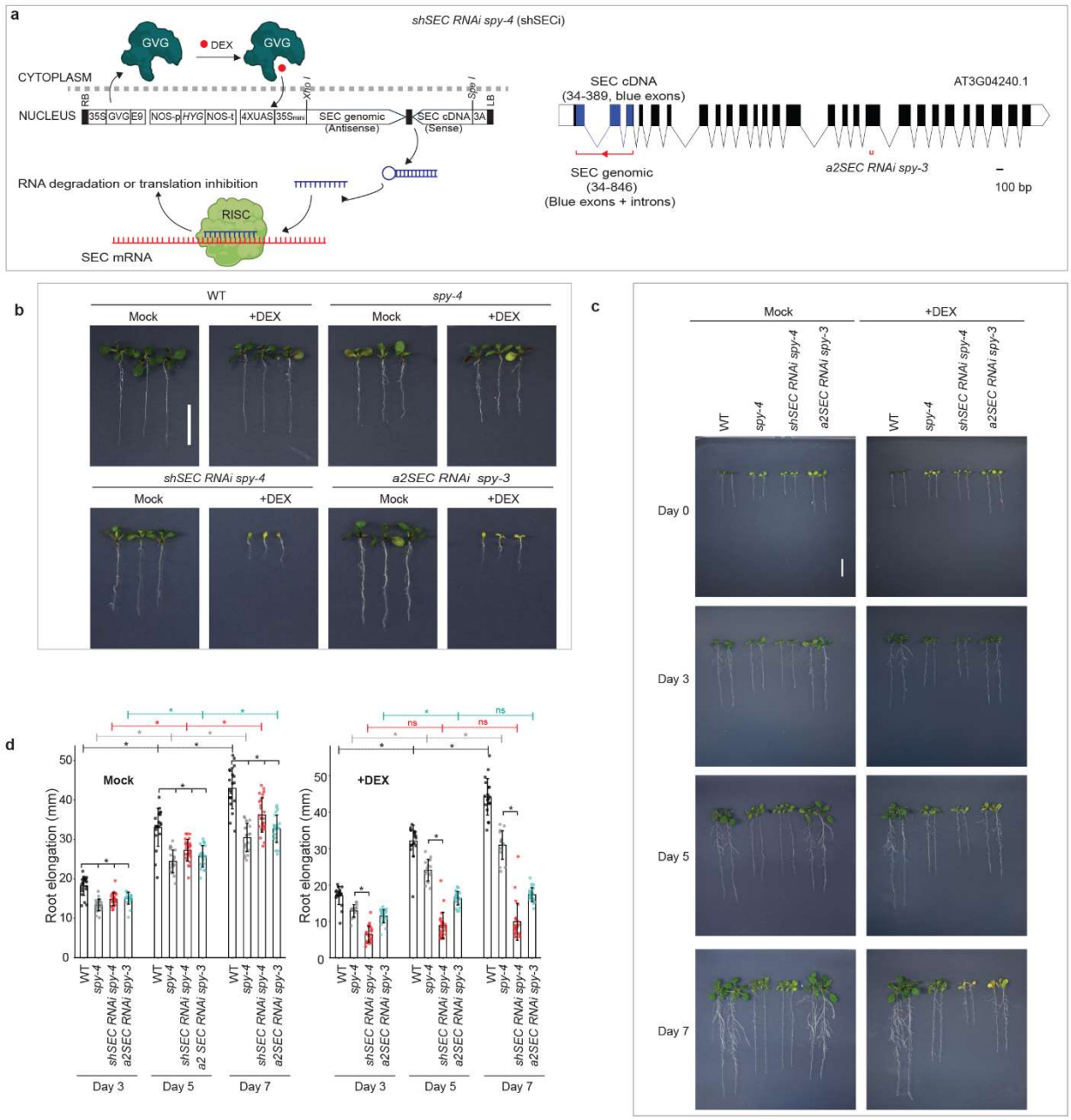

Extended data Fig. 5 | The inducible *shSEC RNAi spy-4* line shows seedling lethality. a. Schematic of Dex-inducible *shSEC RNAi* construct compared to *a2SEC RNAi*. Genomic and cDNA of SEC segments are cloned in a head-to-head orientation to pTA7002 to generate the short hairpin RNAi. **b.** Seedling lethality was observed when double mutants were grown directly on Dex-supplemented plates. **c**. Progressive phenotype of *shSEC RNAi spy-4* phenotype after Dex treatment, showing reduced root growth by day 3, leaf discoloration by day 5 and complete growth arrest by day 7. **d**. Quantification of root elongation after transfer on mock and Dex treatment. Root lengths were measured in over 15 seedlings, and statistical analysis was performed using a two-tailed t-test ($p < 0.001$).

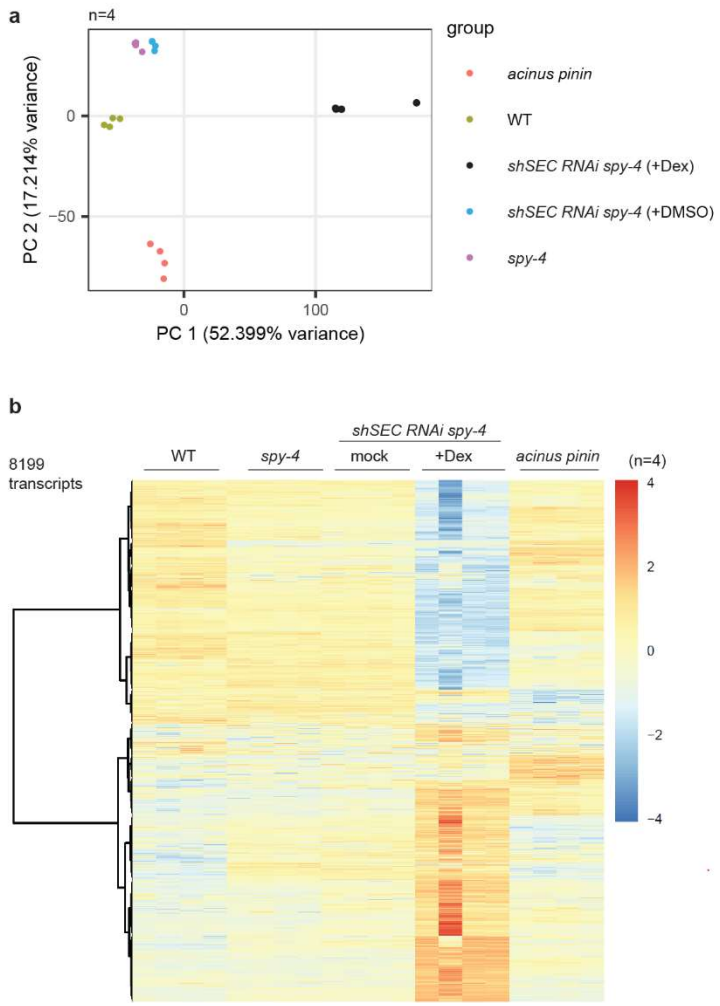

Extended data Fig. 6 | PCA analysis of RNA-seq results and comparison of altered transcript. a. PCA analysis of transcriptomics data from WT, *acinus pinin*, *spy-4*, *shSEC RNAi spy-4* (with and without Dex treatment) shows distinct clustering of each group, as well as clustering between *spy-4* and *shSEC RNAi spy-4* groups. **b**. Heatmap depicting 8199 transcripts that are altered in *acinus pinin*, *shSEC RNAi spy-4* (with Dex), or both.